Nano Research

ISSN 1998-0124 CN 11-5974/O4
https://doi.org/10.26599/NR.2026.94908753

Research Article

Structure and surface co-modified lithium ion-sieve $H_{1.6}Mn_{1.6}O_4$ sub-micron spheres with efficient enhancement in adsorption of lithium from simulated salt lake brine

Aoqun Liu, Shenbo Zhu, Yueyu Ma, Fanli Meng, Quan Zhou, Yuchen Xue, Yinghao Zhao, Xingguang Zhao, Wancheng Zhu(✉)
Department of Chemical Engineering, Qufu Normal University, Qufu 273165, China

Nano Res., **Just Accepted Manuscript** • https://doi.org/10.26599/NR.2026.94908753
https://www.sciopen.com/journal/1998-0124 on Apr. 20, 2026

Just Accepted

Structure and surface co-modified lithium ion-sieve $H_{1.6}Mn_{1.6}O_4$ (HMO-EtOH & SDS) sub-micron spheres consisted of tiny nanoparticles with significantly improved super-hydrophilicity, high equilibrium adsorption capacity (q_e=56.71 mg g^{-1}), fast adsorption rate (t_e=3.0 h) are obtained, bearing a maximum adsorption capacity of 58.74 mg g^{-1}, low manganese dissolution rate (3.57-5.25 wt%), excellent cycling adsorption performance, and high separation coefficients (α_{Mg}^{Li}=412.33, α_{Na}^{Li}=2120.57) for simulated high Mg/Li and especially high Na/Li ratio salt lake brines.

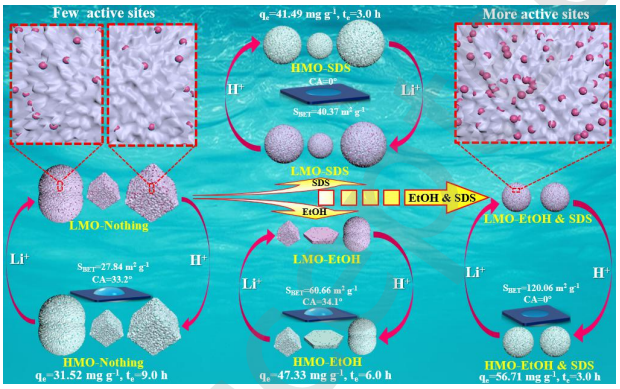

Research Article

Structure and surface co-modified lithium ion-sieve $H_{1.6}Mn_{1.6}O_4$ sub-micron spheres with efficient enhancement in adsorption of lithium from simulated salt lake brine

Aoqun Liu, Shenbo Zhu, Yueyu Ma, Fanli Meng, Quan Zhou, Yuchen Xue, Yinghao Zhao, Xingguang Zhao, and Wancheng Zhu*
Department of Chemical Engineering, Qufu Normal University, Qufu 273165, China

Received: 6 January 2026; **Revised:** 18 April 2026; **Accepted:** 20 April 2026
*Address correspondence to zhuwancheng@tsinghua.org.cn

Cite this article: *Nano Research*, 2026, 19, 94908753
https://doi.org/10.26599/NR.2026.94908753

ABSTRACT

Driven by the rapid growth of new energy vehicles and energy storage, development of lithium extraction technologies from salt lake brines has been considerably stimulated. This work introduces a novel method for structure and surface co-modification of the manganese-based lithium ion-sieve $H_{1.6}Mn_{1.6}O_4$ (HMO-EtOH & SDS) sub-micron spheres, employing ethanol (EtOH) and sodium dodecyl sulfate (SDS) as the additives. The HMO-EtOH & SDS sub-micron spheres exhibit a uniform spherical morphology, narrow size distribution (300-600 nm), small average particle size (0.44 μm), large specific surface area (120.06 $m^2\ g^{-1}$), super-hydrophilicity and relatively rich porous structure. When utilized as the adsorbents, HMO-EtOH & SDS sub-micron spheres demonstrate a high equilibrium adsorption capacity (q_e=56.71 mg g^{-1}) and a fast adsorption rate (t_e=3.0 h), with a maximum adsorption capacity of 58.74 mg g^{-1}. After five cycles of adsorption, an excellent cycling performance (retention rate: 80.23 wt%) and low manganese dissolution rate (below 5.25 wt%) have been accomplished. Additionally, for extraction of lithium from the simulated salt brine, an equilibrium adsorption capacity of 25.41 mg g^{-1} and relatively high separation coefficients (α_{Mg}^{Li}=412.33, α_{Na}^{Li}=2120.57) have also been achieved.

KEYWORDS: lithium extraction, lithium ion-sieve, co-modification, salt lake brine, sub-micron spheres

1 Introduction

The ever-increasing demand for power vehicles and energy storage systems has significantly accelerated the global exploration of lithium resources, which can be found in various geological settings including pegmatites, clays, lithium zeolites, seawater, and salt lake brines[1-6]. However, the extraction of Li from ores is often hampered by the depletion of high-grade deposits, high energy consumption, significant costs, and environmental concerns[7]. While seawater holds about 230 million tonnes of lithium reserves, the extremely low concentration (approximately 0.18 mg L^{-1}) makes extraction economically challenging[8]. In comparison, salt lake brines account for a substantial share of global lithium reserves and present a more feasible source, especially with ongoing technological advances[5].

Several techniques are currently employed for lithium recovery from liquid resources, including co-precipitation[9], nanofiltration[10], electrodialysis[11, 12], solvent extraction[13] and adsorption[14-17]. Among them, co-precipitation is simple and cost-effective but is limited to brines with low Mg/Li ratios[9]. Nanofiltration, a pressure-driven membrane process, struggles to effectively separate Mg^{2+} and Li^{+} due to their similar hydrated radii[10]. Although electrodialysis is an efficient membrane-based electrochemical method, its application is constrained by the availability of membranes with high lithium selectivity[11]. Solvent extraction often employs toxic organic solvents, raising environmental concerns[13]. In contrast, the adsorption method stands out for its high selectivity, operational simplicity, and environmental friendliness, making it a highly promising approach for lithium extraction[5, 15, 16].

In the extraction of Li by adsorption, aluminium-based lithium ion-sieves (HAOs), manganese-based lithium ion-sieves (HMOs) and titanium-based lithium ion-sieves (HTOs) have been widely studied[15, 16, 18]. Among the three kinds of lithium ion-sieves, HAOs have been industrially applied in some cases, however the low capacity limits their broader application[18, 19]. HTOs exhibit excellent stability and relatively high adsorption capacity but are constrained by the intrinsic high cost[16, 20, 21]. Consequently, HMOs have emerged as the promising candidate, due to their high adsorption capacity and low cost[15, 22, 23]. Nevertheless, HMOs face significant challenges including manganese dissolution, a substantial gap between the practical and theoretical capacity (72.3 mg g^{-1}), as well as slow adsorption rate[24, 25]. To address these issues, researchers usually use doping and surface coating methods to improve the adsorption performance of HMOs[26, 27]. Su et al. developed S and Al co-doped $H_{1.6}Mn_{1.6}O_4$ with significantly improved structural

stability, where the Mn dissolution loss was reduced from 5.4% to 3.0%. However, the material exhibited a long adsorption equilibrium time (>8.0 h) and relatively low specific surface area[28]. Zhang et al. realized morphology regulation of HMO microspheres, yet the surface hydrophilicity and porous structure were not optimized, leading to unsatisfactory adsorption rate[29]. Gao et al. prepared Al and Cr co-doped $H_{1.6}Mn_{1.6}O_4$ adsorbent with improved stability, however when compared with the undoped adsorbent, only an increase in the adsorption capacity from 20.3 to 25.5 mg g^{-1} was achieved and the equilibrium was not yet reached after 40.0 h[30]. Zhang et al. coated the surface of the $Li_{1.6}Mn_{1.6}O_4$ with a conductive lanthanum lithium titanate (LLTO) layer, which contained doped lanthanum and titanate as well as residual lithium[31]. This modification led to a decline in the manganese dissolution rate from 2.54 wt% to 1.93 wt% but just with a slight improvement in the adsorption capacity from 31.81 to 35.66 mg g^{-1}, and the time for equilibrium remained almost unchanged[31]. Although the doping and surface coating methods can effectively improve the stability of HMOs, they can hardly simultaneously bring about the promotion in the adsorption capacity and adsorption rate.

In recent years, nanostructure engineering and surface/interface optimization have emerged as powerful strategies for designing high-performance functional materials with effective routes to enhancement in mass transport efficiency[32-35]. As known, larger specific surface area and richer porous structure within adsorbents are instrumental for providing more active sites, thereby increasing the adsorption capacity[23, 36-38]. Additionally, better hydrophilicity facilitates faster attraction of adsorbates, thus promoting the adsorption rate[39, 40].

In this work, enlightened by the above advanced structural design concepts, structure and surface co-modified manganese-based lithium ion-sieve $H_{1.6}Mn_{1.6}O_4$ (HMO-EtOH & SDS) sub-micron spheres with high adsorption capacity and fast adsorption rate have been successfully obtained, by using EtOH and SDS as the additives. The HMO-EtOH & SDS sub-micron spheres exhibit a high adsorption capacity (56.71 mg g^{-1}) and short adsorption equilibrium time (3.0 h), much higher and shorter than those of the unmodified manganese-based lithium ion-sieve HMO-Nothing (31.52 mg g^{-1}, 9.0 h), respectively. The effects of EtOH and SDS on the surface and structure of the adsorbents, and underlying probable mechanisms governing the superior lithium adsorption performance of the HMO-EtOH & SDS sub-micron spheres are uncovered. In addition, comparatively satisfactory cyclic performance with low manganese dissolution rate (below

5.25 wt%) has also been realized. Meanwhile, the as-obtained HMO-EtOH & SDS sub-micron spheres deliver showed remarkably high selectivity (α_{Mg}^{Li}=412.33, α_{Na}^{Li}=2120.57) and Li adsorption capacity (25.41 mg g^{-1}) for Li extraction from the simulated salt lake brine, indicating their great potentials for future lithium extraction from authentic high Mg/Li ratio, especially high Na/Li ratio salt lake brines.

2 Experimental

2.1 Materials and reagents

Detailed information can be found in the **ESI**, as shown by the **Text S1**.

2.2 Synthesis of $MnCO_3$ and MnO_2 sub-micron spheres

In the first place, $MnCO_3$ sub-micron spheres were synthesized by a co-precipitation method. Specifically, 1.69 g of $MnSO_4{\cdot}H_2O$ and 3.95 g of NH_4HCO_3 were individually dissolved in respective 500 mL of deionized (DI) water. Then the NH_4HCO_3 solution was quickly poured into the $MnSO_4{\cdot}H_2O$ solution, and the resultant slurry was magnetically stirred at 500 rpm for 30 min. After that, the original $MnCO_3$ powder was obtained by filtering, washing with DI water and drying at 80 ºC for 3.0 h. To see the possible effects of surfactant and solvent, during co-precipitation process, surfactant sodium dodecyl sulfate (SDS) was introduced into the NH_4HCO_3 solution, with the mass ratio of SDS to $MnSO_4{\cdot}H_2O$ kept as 0-60 wt%. Simultaneously, pure DI water was tuned to the mixed solvent bearing anhydrous ethanol (EtOH) and DI water, with the volume ratio of EtOH to DI water preset as 1:4-1:1.

The as-obtained $MnCO_3$ was then stepwise calcined for MnO_2. Typically, $MnCO_3$ powder was shifted to a porcelain boat, which was located in a horizontal tube furnace. The furnace was originally heated to 200 ºC (ramp rate: 5 ºC min^{-1}), then to 400 ºC (ramp rate: 2 ºC min^{-1}) and kept in an isothermal state, followed by a natural cooling down to room temperature. Subsequently, MnO_2 powder was collected.

2.3 Transformation to LMOs and HMOs sub-micron spheres

Further procedures for the synthesis of lithium ion-sieve precursors (LMOs) consisted of the following steps. Firstly, 1.305

g of MnO_2 powder was put into a mortar, 5 ml of anhydrous EtOH was taken to disperse the MnO_2, and then 1.224 g of $LiOH{\cdot}H_2O$ was introduced (with 10 mol% of excess corresponding to that of MnO_2). MnO_2 and $LiOH{\cdot}H_2O$ were mixed and ground until eventual volatilization of EtOH, The resultant black powder within the mortar was subsequently put into an oven and further dried at 80 ºC for 5.0 h. Secondly, the black powder was carefully scraped off the mortar and transferred into a Teflon-lined autoclave, which was heated to and remained at 120 ºC for 24.0 h. Eventually, LMOs were obtained by calcining the above hydrothermal product at 500 ºC for 4.0 h in air (heating rate: 5 ºC min^{-1}). To see the possible effect of chemical composition of the LMOs on the adsorption capacity, the molar ratio of $LiOH{\cdot}H_2O$ to MnO_2 was adjusted to 1:2, 4:5, 2:1, and 1:1, respectively, with other conditions kept the same.

In addition to $LiOH{\cdot}H_2O$, Li_2CO_3 was also employed as the lithium source to see the possible effect. $LiOH{\cdot}H_2O$ and Li_2CO_3 derived LMOs were individually named as LMO-LiOH and LMO-Li_2CO_3. Besides, to ascertain the probable effects of SDS and EtOH on the LMOs, a series of LMOs were synthesized. LMOs those originated from neither SDS nor EtOH, only SDS, only EtOH, both SDS and EtOH were denoted as LMO-Nothing, LMO-SDS, LMO-EtOH and LMO-EtOH & SDS, respectively.

To get HMOs sub-micron spheres, the LMOs synthesized above were washed with acid. Specifically, the fresh powder of LMOs was treated with a 0.2 M of HCl at 50 ºC for 4.0 h, washed sequentially with DI water and EtOH, and then dried at 80 ºC for 3.0 h. Correspondingly, HMOs initiated from the above LMOs were further individually designated as HMO-LiOH, HMO-Li_2CO_3, HMO-Nothing, HMO-SDS, HMO-EtOH, and HMO-EtOH & SDS. A schematic illustration of the whole synthetic process for HMOs was shown in **Scheme 1**.

2.4 Adsorption performances of HMOs

To evaluate adsorption performances and further compare the adsorption capacities of various HMOs, a series of experiments were conducted. In each experiment, 0.2 g of the adsorbent was added to 100 mL of a lithium solution (derived from $LiOH{\cdot}H_2O$) with a pH of 12.0 and an initial concentration of 1.8 g L^{-1}, and the adsorption was carried out at a temperature of 35 ºC. To optimize the experimental conditions, 1.0 mL of the suspension was sampled at predetermined time intervals from adsorption system and filtered using a disposable syringe needle filter (diameter: 13.0 mm, pore size:

0.22 μm). The concentration of lithium ions (Li^+) in the filtrate was determined. Adsorption uptakes of Li^+ of specific HMOs at equilibrium and any time t were calculated by the following **eqns. (1)** and **(2)**, respectively[26].

$$q_e = \frac{(C_0 - C_e) \times V}{m} \quad (1)$$

$$q_t = \frac{(C_0 - C_t) \times V}{m} \quad (2)$$

where q_e (mg g^{-1}) and q_t (mg g^{-1}) are the adsorption uptakes of the HMOs at equilibrium and any time t, respectively; C_0 (mg L^{-1}) is the initial lithium ion concentration within the Li^+ solution; C_e (mg L^{-1}) and C_t (mg L^{-1}) are individually the Li^+ concentrations within the solution at equilibrium and any time t; V (L) is the volume of solution; m (g) is the mass of the HMOs.

2.5 Effects of pH and temperature on adsorption capacity

Detailed information on the influences of pH and temperature can be found in the **ESI**, as shown by the **Text S2** and **Text S3**, respectively.

2.6 Adsorption isothermal behavior and adsorption kinetics

To investigate the adsorption isothermal behavior of lithium ions during the adsorption process，HMO-EtOH & SDS was dispersed in solutions with the concentration of lithium varying within the range of 100-2000 mg L^{-1}. The system was magnetically stirred for 12.0 h. Subsequently, the experimental data were fitted by the adsorption isothermal models, such as the Langmuir and Freundlich isotherm models, which can be expressed by **eqns. (3)** and **(4)**, respectively[23, 41].

$$q_e = \frac{q_m K_L C_e}{1 + K_L C_e} \quad (3)$$

$$q_e = K_f C_e^{1/n} \quad (4)$$

of which q_m (mg g^{-1}) is the maximum adsorption capacity; K_L (L mg^{-1}) denotes the coefficient related to binding site affinity; K_f and 1/n represent the correlation constants of adsorption amount and adsorption strength per unit concentration, respectively.

To elucidate the adsorption dynamics and reaction mechanism, the adsorption capacity of HMO-EtOH & SDS was measured at various time intervals throughout the lithium-ion adsorption process. The collected data were fitted by the

pseudo-first-order (PFO) and pseudo-second-order (PSO) kinetic models, which can be individually expressed by the **eqns. (5)** and **(6)**[23, 41].

$$\ln (q_e - q_t) = \ln q_e - k_1 t \quad (5)$$

$$\frac{t}{q_t} = \frac{1}{k_2 q_e^2} + \frac{t}{q_e} \quad (6)$$

where k_1 (h^{-1}) is the adsorption rate constant for the quasi-primary kinetic equation; k_2 (g (mg h)$^{-1}$) is the adsorption rate constant for the quasi-secondary kinetic equation.

Also, to better understand the surface diffusion of HMO-EtOH & SDS, we used the intra-particle diffusion model and Boyd model. Of which, the intra-particle diffusion model is presented as **eqn. (7)**[23, 37, 38, 41].

$$q_t = K_d \cdot t^{1/2} + I \quad (7)$$

here K_d (mg (g $h^{1/2}$)$^{-1}$) is the rate constant, and I is the intercept.

Meanwhile, the Boyd model is denoted as **eqn. (8)**[23, 37, 38, 41].

$$F = q_t/q_e \quad (8)$$

in which F is the fraction of the solute adsorbed at any time. The Boyd model can be approximated as **eqns. (9)** and **(10)**[23, 37, 38, 41].

$$F > 0.85{:}Bt = -0.4997 - ln(1 - F) \quad (9)$$

$$F < 0.85{:}Bt = \sqrt{\pi} - \sqrt{\pi - \frac{\pi^2 F}{3}} \quad (10)$$

where Bt represents the time constant, also a mathematical function of F.

2.7 Cycling performances

Typically, 1 g of the HMO-EtOH & SDS was put into 250.0 mL of the lithium solution and then magnetically stirred at 35 ºC for 12.0 h. After each adsorption cycle, the resultant LMO-EtOH & SDS was pickled in 50 mL of the HCl solution (0.2 M) at 50 ºC for 4.0 h, and the regenerated HMO-EtOH & SDS was then dried at 50 ºC for 12.0 h[23]. The pickler was collected for Mn^{2+} analysis. In total, five successive adsorption cycles were performed to evaluate the recyclability of the HMO-EtOH & SDS. For comparison, the HMO-Nothing was substituted for HMO-EtOH & SDS, with other conditions

kept the same.

2.8 Adsorption selectivity of Li^+ in simulated salt lake brine

To see the potential practicability of the adsorbent HMO-EtOH & SDS, the simulated salt lake brine according to the composition of the authentic brine of the West Taijinar Salt Lake, Qinghai province of China was employed for evaluation at 35 ºC for 12.0 h. After reaching adsorption equilibrium, the contents of Li^+, Na^+, K^+, Ca^{2+}, and Mg^{2+} were analyzed. The distribution coefficient (K_d) and the separation coefficient (α_M^{Li}), indicative of the adsorption capacities of lithium and other ions, were individually calculated using **eqns. (11)** and **(12)**[23].

$$K_d = \frac{(C_0 - C_e) \times V}{C_e \times W} \quad (11)$$

$$\alpha_M^{Li} = \frac{K_{Li}}{K_d} \quad (12)$$

Of which C_0 (mg L^{-1}) and C_e (mg L^{-1}) represent the initial and equilibrium concentrations of cations, respectively, V (mL) denotes the solution volume, and W (g) stands for the weight of the adsorbents.

2.9 Characterizations

Detailed information can be found in the **ESI**, as shown by the **Text S4**.

3 Results and discussions

3.1 Composition and morphology of the LMO-EtOH & SDS and HMO-EtOH & SDS

The composition and microstructure of the hydrothermal product, LMO-EtOH & SDS and HMO-EtOH & SDS were shown in **Fig. 1**. As can be seen, the hydrothermal product (**Fig. 1(a_1)**) can be readily indexed to $LiMnO_2$ (JCPDS No.35-0749)[25]. Apparently, the XRD patterns of the LMO-EtOH & SDS (**Fig. 1(a_2)**) and HMO-EtOH & SDS (**Fig. 1(a_3)**) display the characteristic diffraction peaks at 18.8°, 36.5°, 44.5°, 58.9° and 64.7°, which can be indexed to the (111), (311), (400), (511), and (440) crystalline planes of the $Li_{1.6}Mn_{1.6}O_4$ (JCPDS No.52-1841), respectively[41]. It is noteworthy that the HMO-EtOH & SDS, obtained by acid washing of LMO-EtOH & SDS, retains the cubic spinel structure, except for a slight shift of the characteristic peaks to higher Bragg angles with a reduction in the diffraction intensities. This is due to the fact

that the effective ionic radius of H^+ is smaller than that of Li^+ in the process of desorption[22]. As shown by the SEM image (**Fig. S1(a)**), the hydrothermal product particles are of distinct sub-micron spheres (average diameter: 0.44 μm). Meanwhile, both the LMO-EtOH & SDS (**Fig. S1(b)**) and HMO-EtOH & SDS (**Fig. 1 (b)**) exhibit similar morphology, which are tiny nanoparticles (NPs) constituted submicron-spheres with high dispersion, narrow size distribution (300-600 nm) and average diameters of 0.45 μm and 0.44 μm, respectively. In addition, the TEM and the inset HRTEM images further demonstrate (**Fig. 1(c, c1)**) that the HMO-EtOH & SDS is a monodisperse sphere and the detected interplanar spacing from the lattice fringes is 0.472 nm, which well corresponds to the standard value of the (111) planes for the crystalline cubic spinel $Li_{1.6}Mn_{1.6}O_4$[42]. Meanwhile, the EDS spectrum results for the HMO-EtOH &SDS (**Fig. 1(d)**) indicates that the molar ratio of O:Mn is 2.53:1, quite analogous to the stoichiometric molar ratio of O:Mn for $Li_{1.6}Mn_{1.6}O_4$ (2.5:1). And also, as depicted in **(Fig. 1(e, f)**, the elemental mappings demonstrate the presence as well as the uniform distribution of Mn and O within the sub-micron spheres.

3.2 Preparation conditions for the $MnCO_3$ and MnO_2 sub-micron spheres

3.2.1 Influence of SDS on the $MnCO_3$

As shown by the XRD patterns in **Fig. S2(a)**, as the mass ratio of SDS to $MnSO_4 \cdot H_2O$ varying within the range of 0-60 wt%, all samples can be indexed to the pure phase of $MnCO_3$ (JCPDS No. 44-1427)[43]. Neither significant change in the diffraction intensities nor variation in the peak positions can be observed. Thus, the introduction of SDS did not influence the crystal structure of the $MnCO_3$. Meanwhile, relatively evident change in the morphology of the $MnCO_3$ has been confirmed. As the SEM images (**Fig. S2(b-f)**) shown, when no SDS was used, rudimental $MnCO_3$ microspheres accompanied by cubes were formed (**Fig. S2(b, b_1)**), with a diameter of 0.13-2.76 μm (average: 1.74 μm). With the mass ratio of SDS to $MnSO_4 \cdot H_2O$ increasing from 30 wt% (**Fig. S2(c, c_1)**) to 40 wt% (**Fig. S2(d, d_1)**) to 50 wt% (**Fig. S2(e, e_1)**), smaller and smaller $MnCO_3$ microspheres with less and less cubes were acquired, with a diameter decreasing from 0.11-2.73 μm (average: 1.53 μm) to 0.01-2.15 μm (average: 1.50 μm) to 0.12-1.93 μm (average: 1.36 μm). This indicates that SDS is prone to form micelles, which is conducive to promoting the spheroidization of $MnCO_3$[43]. Nevertheless, with

the mass ratio of SDS to $MnSO_4 \cdot H_2O$ further goes up to 60 wt% (**Fig. S2(f, f_1)**), the diameter ascends to 0.13-2.36 μm (average: 1.71 μm). Obviously, the morphology and size of the $MnCO_3$ can be well controlled by tuning the mass ratio of SDS to $MnSO_4 \cdot H_2O$. And with the mass ratio of SDS to $MnSO_4 \cdot H_2O$ set as 50 wt%, the $MnCO_3$ microspheres exhibit the narrowest size distribution and smallest average diameter.

3.2.2 Effect of volume ratio of EtOH to H_2O on the $MnCO_3$

In the presence of the mass ratio of SDS to $MnSO_4 \cdot H_2O$ as 50 wt%, XRD patterns of the $MnCO_3$ derived from different volume ratio of EtOH to H_2O were displayed in **Fig. S3(a).** Clearly, all samples are pure phase of the $MnCO_3$ (JCPDS No. 44-1472)[43], and there's a slight increase in the crystallinity with the increase in the volume ratio of EtOH to H_2O from 1:4 (**Fig. S3(a_1)**) to 1:3 (**Fig. S3(a_2)**) to 1:2 (**Fig. S3(a_3)**) and 1:1 (**Fig. S3(a_4)**). And simultaneously, with such variation in the volume ratio EtOH to H_2O, the diameter distributions were confirmed as 0.10-0.95 μm (**Fig. S3(b, b_1)**, average: 0.55 μm), 0.11-0.86 μm (**Fig. S3(c, c_1)**, average: 0.43 μm), 0.13-0.89 μm (**Fig. S3(d, d_1)**, average: 0.52 μm), 0.09-0.98 μm (**Fig. S3(e, e_1)**, average: 0.64 μm), respectively. Taking the narrowest size distribution (i.e. spherical uniformity) and smallest average diameter into consideration, the volume ratio of EtOH to H_2O is determined as 1:3 hereafter.

3.2.3 Thermal conversion conditions for the MnO_2

After the thermal conversion, relatively low crystallinity MnO_2 (JCPDS No. 30-0820) sub-micron spheres (**Fig. S4(a, b)**) have been obtained[44], with the spherical morphology well preserved from that of the $MnCO_3$ (**Fig. S3(c, c_1)**). The MnO_2 sub-micron spheres demonstrate a diameter of 300-600 nm (**Fig. S4(b, b_1)**, average: 0.41μm). Since the MnO_2 sub-micron spheres consist of tiny NPs, the possible porous structure was further characterized. The corresponding N_2 adsorption–desorption isotherms (**Fig. S4(c)**) exhibit a type-IV profile containing an H3 hysteresis loop (IUPAC classification) within the relative pressure (p/p_0) range of 0.75–1.0, and the pore diameter distribution curve (**Fig. S4(c_1)**) indicates that the MnO_2 sub-micron spheres bear abundant micropores and mesoporous as well as few macropores. In addition, the porous structure reveals that the MnO_2 sub-micron spheres have a specific surface area of 168.61 $m^2 g^{-1}$, an average pore diameter of 38.22 nm and a total pore volume of 3.15 $cm^3 g^{-1}$ (**Table S1**). This suggests the MnO_2 sub-micron spheres as ideal precursors for the next synthesis of LMO when appropriate Li source is introduced under proper conditions.

3.3 Transformation to the LMOs and HMOs

3.3.1 Adsorption capacities of HMOs with different compositions

As the XRD patterns shown in **Fig. S5(a)**, simply tuning the molar ratio of $LiOH{\cdot}H_2O$ to MnO_2 as 1:2, 4:5, 2:1, and 1:1, four LMOs of $LiMn_2O_4$ (**Fig. S5(a_1)**, JCPDS No.53-1327)[45], $Li_{1.33}Mn_{1.67}O_4$ (**Fig. S5(a_2)**, JCPDS No.46-0810)[46], Li_2MnO_3 (**Fig. S5(a_3)**, JCPDS No.27-1252)[47] and $Li_{1.6}Mn_{1.6}O_4$ (**Fig. S5(a_4)**, JCPDS No.52-1841)[41] have been obtained, respectively. Next, four LMOs were washed by HCl, DI water and EtOH, and then finally dried. The resultant HMOs (i.e. HMn_2O_4, $H_{1.33}Mn_{1.67}O_4$, H_2MnO_3 and $H_{1.6}Mn_{1.6}O_4$) were preliminarily deployed for adsorption of Li^+ from LiOH solution, the results were shown in **Fig. S5(b)**. Obviously, all of the four HMOs exhibit lithium uptakes greater than 20 mg g^{-1}, indicating their relatively satisfactory adsorption capacities for Li^+. Notably however, of the four HMOs, $H_{1.6}Mn_{1.6}O_4$ (**Fig. S5(b_4)**) has revealed the largest adsorption capacity. Thus $Li_{1.6}Mn_{1.6}O_4$ is more ideal for the recovery of Li^+ from Li-containing solution, consistent with the findings of Sun et al. **Table S2** summarizes the structures of the four LMOs as well as the valence states of Mn. As tabulated, $Li_{1.6}Mn_{1.6}O_4$, $Li_{1.33}Mn_{1.67}O_4$ and $LiMn_2O_4$ are all spinel structures belonging to the cubic crystalline system with the space group of Fd3m, which has a high degree of symmetry[48]. Although the three precursors belong to the spinel structure, the different Li-Mn ratios result in some differences in the position of Li and Mn within the three-dimensional space. Li_2MnO_3 is a layered structure with certain gaps or intervals between each layer, the layers are connected by van der Waals forces or other weak interactions and the atoms within the layers are more tightly arranged[23]. Thus, the differences in structure and valence of Mn might have to some extent led to the variation in the adsorption capacities of the four HMOs.

3.3.2 Influence of Li sources on HMOs

To investigate the impact of various Li sources on the morphology and adsorption capacity of the HMOs, the most commonly used Li_2CO_3 and $LiOH{\cdot}H_2O$ were chosen as the Li sources, and the XRD patterns of the resultant samples (LMO-Li_2CO_3 and LMO-LiOH) were individually displayed in **Fig. S6(a_1)** and **Fig. S6(a_2)**. Clearly, all of them are pure phase of $Li_{1.6}Mn_{1.6}O_4$ (JCPDS No. 52-1841)[41]. After acid washing, the as-obtained two HMOs were employed for

adsorption of Li^+. It is obvious that, the HMO-Li_2CO_3 (**Fig. S6(b_1)** exhibits a lithium uptake distinctly lower than HMO-LiOH (**Fig. S6(b_2)** does. In order to better understand the reasons affecting the adsorption capacity, the significant effect of different lithium sources on the morphology of the product was also investigated. As shown in **Fig. S6(c)**, it can be clearly seen that HMO-Li_2CO_3 consists of both lumpy and spherical particles. When Li_2CO_3 was used as the lithium source and physically mixed with MnO_2, the larger size of Li_2CO_3 might hinder its effective incorporation into the surface grooves of the MnO_2 during the calcination process. Additionally, the release of CO_2 from Li_2CO_3 during the calcination would inevitably result in the destruction of the surface structure of LMOs and resultant HMOs. In contrast, when $LiOH{\cdot}H_2O$ was deployed as the lithium source **(Fig. S6(d))**, no CO_2 was released. This can reduce the damage to the structure of the MnO_2, and thus enabling the LMOs and subsequent HMOs with preserved spherical morphology and constitutional porous structure. The specific porous structure of HMO-LiOH guarantees more active sites, which contributes a better adsorption performance (**Fig. S6(b_2)**) superior to that of HMO-Li_2CO_3 (**Fig. S6(b_1)**. Consequently, $LiOH{\cdot}H_2O$ was chosen as the ideal lithium source hereafter.

3.3.3 Effects of SDS and EtOH on the HMOs

Above, it has been found that the molar ratio of SDS to $MnSO_4{\cdot}H_2O$ and the volume ratio of EtOH to H_2O can largely affect the composition, morphology and diameter distribution of the $MnCO_3$ and also the resultant MnO_2. As a consequence, the properties of the obtained HMOs, including crystallinity, pore structure, specific surface area and hydrophilicity, were also influenced. **Fig. 2(a)** shows the XRD patterns of the four lithium ion-sieve precursor samples, which can all be readily indexed to those of the standard $Li_{1.6}Mn_{1.6}O_4$ (JCPDS No.52–1841)[41]. As can be seen, compared with LMO-Nothing (**Fig. 2(a_1)**), other three LMOs (LMO-SDS (**Fig. 2(a_2)**), LMO-EtOH (**Fig. 2(a_3)**), LMO-EtOH & SDS (**Fig. 2(a_4)**)) with lower crystallinity were obtained. Decrease in the crystallinity to a large degree indicates the probable modification effects of SDS and EtOH on the LMO.

As shown in **Fig. 2(b, c),** defined by IUPAC, all lithium ion-sieve samples of HMOs (HMO-Nothing (**Fig. 2(b_1)**), HMO-SDS (**Fig. 2(b_2)**), HMO-EtOH (**Fig. 2(b_3)**) and HMO-EtOH & SDS (**Fig. 2(b_4)**)) exhibit irreversible type IV adsorption isotherms, with distinct H3 type hysteresis loops within the relative pressure range of 0.9-1.0, 0.75-1.0, 0.6-0.95,

0.45-95, respectively. And also, HMO-EtOH & SDS (**Fig. 2(b_4)**) reveals more abundant mesopores within the structure. Meanwhile, the pore diameter distribution (**Fig. 2(c)**) also demonstrates remarkable mesopores within the HMO-EtOH & SDS (**Fig. 2(c_4)**). The specific surface area, average pore diameter and total pore volume of the four HMOs were given in **Table S3**. Compared with the HMO-Nothing, HMO-SDS and HMO-EtOH and HMO-EtOH & SDS reveal larger and larger specific surface area, average pore diameter and total pore volume, and of which HMO-EtOH & SDS bears the largest value of the porous structure parameters. This indicates the greater contribution of EtOH than SDS, and especially the coexistence of EtOH and SDS has made the greatest contribution to the conspicuous promotion in the specific surface area (120.06 m^2 g^{-1}), pore diameter (24.68 nm) and pore volume (0.1748 cm^3 g^{-1}), to a large degree confirming the synergistic effects of EtOH and SDS on the increase in the porous structure.

Meanwhile, the morphologies of the four samples are significantly different. HMO-Nothing (**Fig. 2(d)**) particles with quasi-spherical or quasi-cubic morphology and wide size distribution (100 nm-2 μm) constituted of column- or plate-like subunits were obtained. For clarity, representative particle sizes (e.g. 0.98 μm, 0.77 μm, and 0.32 μm) are labeled in **Fig. 2(d)**, with the aim to visualize the broad size distribution of the particles. In contrast, after the addition of SDS, distinctly regular HMO-SDS (**Fig. 2(e)**) microspheres or sub-micron spheres with a little broad diameter distribution (300 nm-1.2 μm, average diameter: 0.74 μm) containing tiny NPs were acquired. This is to some extent similar to the effect of SDS on the formation of the spherical $H_{1.6}Mn_{1.6}O_4$. And also, irregular HMO-EtOH (**Fig. 2(f)**) particles including predominant sub-micron spheres, a few columns and sporadic nanoplates were obtained. Typical particle sizes (e.g. 0.72 μm, 0.46 μm, and 0.36 μm) are labeled (**Fig. 2(f)**), confirming the as-obtained somewhat smaller sub-micron spheres than those observed within the HMO-Nothing (**Fig. 2(d)**). In contrast, HMO-EtOH & SDS (**Fig. 1(b)**) particles exhibit uniform spherical morphology, relatively smaller average diameter with narrow diameter distribution, and good dispersion. This indicates that EtOH and SDS have jointly exerted an effect on the improvement in the spherical morphology, reduction in the diameter of the spheres, and promotion in the dispersion. This well-dispersed sub-micron spherical lithium-ion sieve can be better dispersed in the Li^+-containing solution with more exposed active adsorption sites, thus shortening the diffusion path of Li^+ and improving the adsorption performance.

Based on our aforementioned discussion and the data presented in **Fig. S2(a_4)**, **Fig. S3(a_2)**, **Fig. S4(a)** and **Fig. 1(a_1-a_3)**, the formation process of the lithium ion-sieve HMO-EtOH & SDS can thus be chemically expressed in the following **eqns. (13-17)**. As can be seen, the whole synthesis follows a sequential process, which includes co-precipitation for $MnCO_3$, subsequent thermal oxidation for MnO_2, hydrothermal conversion and next calcination to form lithium ion-sieve precursor spinel $Li_{1.6}Mn_{1.6}O_4$ (LMO-EtOH & SDS), and acid washing to obtain lithium ion-sieve $H_{1.6}Mn_{1.6}O_4$ (HMO-EtOH & SDS). The spherical morphology is well preserved throughout the entire transformation process.

$$2NH_4HCO_3 + MnSO_4 \rightarrow MnCO_3 \downarrow + H_2O + CO_2 \uparrow + (NH_4)_2SO_4 \quad (13)$$

$$2MnCO_3 + O_2 \rightarrow 2MnO_2 + 2CO_2 \quad (14)$$

$$4MnO_2 + 4LiOH \cdot H_2O \rightarrow 4LiMnO_2 + 6H_2O + O_2 \quad (15)$$

$$8LiMnO_2 + 2O_2 \rightarrow 5Li_{1.6}Mn_{1.6}O_4(LMO - EtOH\ \&\ SDS) \quad (16)$$

$$Li_{1.6}Mn_{1.6}O_4(LMO - EtOH\ \&SDS) + H^+ \rightarrow H_{1.6}Mn_{1.6}O_4(HMO - EtOH\ \&SDS) + Li^+ \quad (17)$$

3.4 Adsorption performance of the HMOs and optimization of the HMO-EtOH & SDS

3.4.1 Evaluation on the adsorption rate of the HMOs

As can be seen, the lithium uptake of the HMO-Nothing (**Fig. 3(a_1)**) goes up steadily within the first 9.0 h and then levels off at 31.52 mg g^{-1}. Comparatively, the lithium uptake of the HMO-SDS (**Fig. 3(a_2)**) increases quickly within the original 3.0 h and gradually turns to steady at 41.49 mg g^{-1}. Similarly, the lithium uptake of the HMO-EtOH (**Fig. 3(a_3)**) ascends rapidly within the initial 6.0 h and then tends to be 47.33 mg g^{-1}. Conspicuously, the lithium uptake of the HMO-EtOH & SDS (**Fig. 3(a_4)**) climbs up abruptly within the premier 1.0 h and promptly becomes stable after 3.0 h at approximate 56.71 mg g^{-1} (i.e. equilibrium adsorption capacity). Thus apparently, in contrast with the former three HMOs (**Fig. 3(a_1-a_3)**), the HMO-EtOH & SDS (**Fig. 3(a_4)**) exhibits both the fastest adsorption rate and the highest equilibrium adsorption capacity. This to some extent confirms our aforementioned discussion (**Fig. 2**), the probable effects of crystallization, specific surface area, and porous structure on the adsorption rate and equilibrium adsorption capacity of the HMOs. As a matter of fact,

lower crystallinity, high specific surface area and abundant porous structure are beneficial for the exposure of more active sites, which can significantly shorten the diffusion path and also facilitate the insertion and removal of the adsorbate.

3.4.2 Zeta potential and impact of initial pH on the adsorption capacity of HMO-EtOH & SDS

To achieve better adsorption capacity of Li^+, zeta potentials of the HMO-EtOH & SDS at different pH values were tested. As depicted in **Fig. 3(b)**, the zeta potential of the HMO-EtOH & SDS descends from 3.1 mV to 1.6 mV with the increase in the pH from 5.3 to 6.5, then rapidly declines to -42.4 mV when the pH goes up to 11.7, and subsequently tends to be stable at *ca.* -43.0 mV. Based on the zeta potentials, the equilibrium adsorption capacities of the HMO-EtOH & SDS for Li^+ at different pH values were investigated. As depicted in **Fig. 3(c)**, significantly, the equilibrium adsorption capacity of the HMO-EtOH & SDS for Li^+ increases slowly with the increase in pH from 5.3 to 6.4, which however rises abruptly within the pH range of 6.4-11.0 and then levels off at approximately 57.0 mg g^{-1}. The zeta potential results further and clearly reveal the electrostatic interaction mechanism for Li^+ adsorption. When pH>6.5, the surface of HMO-EtOH & SDS becomes negatively charged, which provides strong electrostatic attraction to Li^+ and facilitates its adsorption. Meanwhile, the high concentration of OH^- under alkaline conditions neutralizes H^+ on the adsorbent surface, and thus reducing competitive adsorption between H^+ and Li^+ by the adsorbents. These two effects jointly enhance the Li^+ uptake capacity and are well consistent with the adsorption performance observed at different pH values[49, 50]. Apparently, changes in equilibrium adsorption capacity closely correspond to zeta potentials of the HMO-EtOH & SDS, to a large degree indicating their correlation.

3.4.3 Effect of temperature on the adsorption capacity of the HMO-EtOH & SDS

Fig. 3(d) illustrates the variation in the lithium uptakes onto the lithium ion-sieve HMO-EtOH & SDS as a function of time at different temperatures, and under the initial pH value of 12. As indicated, the time required to reach adsorption equilibrium of the HMO-EtOH & SDS decreases with increasing temperature from 25 ºC (**Fig. 3(d_1)**) to 30 ºC (**Fig. 3(d_2)**) then to 35 ºC (**Fig. 3(a_4)**). Meanwhile, within the controlled experimental temperature range, the adsorption at 35 ºC (**Fig. 3(a_4)**) exhibits the highest adsorption capacity of Li^+ onto the HMO-EtOH & SDS.

3.5 Analysis on the contact angle of the HMOs

As depicted in **Fig. S7(a)**, the lithium ion-sieve HMO-Nothing exhibits hydrophilic characteristic, with a surface water contact angle of 33.2°. When SDS was added (mass ratio of SDS to $MnSO_4 \cdot H_2O$= 50 wt%), the surface water contact angle of the HMO-SDS (**Fig. S7(b)**) decreases to 0°, indicating the distinct super-hydrophilicity. This is due to the introduction of hydrophilic groups on the $H_{1.6}Mn_{1.6}O_4$ by the SDS. However, with the addition of EtOH (volume ratio of EtOH to H_2O = 1:3), there is no significant change in the surface water contact angle of HMO-EtOH (**Fig. S7(c)**). This indicates that the addition of EtOH does not affect the hydrophilicity of $H_{1.6}Mn_{1.6}O_4$. In addition, when both SDS and EtOH (mass ratio of SDS to $MnSO_4 \cdot H_2O$= 50 wt%, volume ratio of EtOH to H_2O= 1:3) were added, the surface water contact angle of HMO-EtOH & SDS (**Fig. S7(d)**) exhibits the same super-hydrophilicity as the HMO-SDS (**Fig. S7(b)**), confirming that only SDS contributes to the enhancement in the hydrophilicity. The super-hydrophilic samples (HMO-SDS and HMO-EtOH & SDS) also display the fastest Li^+ adsorption rates in this work (**Fig. 3(a_2)** and **Fig. 3(a_4)**). Therefore, a more hydrophilic adsorbent surface will further accelerate Li^+ exchange with H^+ of $H_{1.6}Mn_{1.6}O_4$.

3.6 Isothermal adsorption and maximum adsorption capacity of Li^+ on the HMO-EtOH & SDS sub-micron spheres

Langmuir and Freundlich isotherm models were used to fit the equilibrium adsorption capacity data for Li^+ onto the HMO-EtOH & SDS sub-micron spheres, as shown in **Fig. 4**, and corresponding fitted parameters were listed in **Table 1**. As can be seen, for the HMO-EtOH & SDS sub-micron spheres, the correlation coefficient R^2 via the Langmuir model is 0.9907 (**Fig. 4(a)**), distinctly higher than that originated from the Freundlich model (0.8361) (**Fig. 4(b)**). Consequently, instead of the Freundlich model, the adsorption data for HMO-EtOH & SDS are better described by the Langmuir model, suggesting a monolayer adsorption process on the HMO-EtOH & SDS sub-micron spheres[23, 41]. Furthermore, the maximum adsorption capacity (q_m) of the HMO-EtOH & SDS sub-micron spheres can be determined as 58.74 mg g^{-1} according to the **eqn. (3)**.

3.7 Adsorption kinetics for Li^+ on the HMO-EtOH & SDS sub-micron spheres

The adsorption kinetics of Li^+ on HMO-EtOH & SDS sub-micron spheres were investigated by fitting the experimental data

to the PFO and PSO models. As shown in **Fig. 5** and **Table S4**, compared with the fitting results by the PFO model (R^2=0.9763, **Fig. 5 (a)**), the PSO model exhibits a better fit and a higher correlation coefficient (R^2=0.9989, **Fig. 5 (b)**). Moreover, the calculated q_{e2} (57.83 mg g^{-1}) of the PSO is obviously closer to the corresponding experimental q_e (56.71 mg g^{-1}) than the q_{e1} (40.74 mg g^{-1}) initiated from the PFO. This definitely manifests the reliability of the PSO rather than the PFO model for the description on the adsorption behavior of Li^+ on the HMO-EtOH & SDS sub-micron spheres. To further investigate the diffusion mechanism, the intra-particle diffusion model was applied. The plot of q_t versus $t_{1/2}$ was shown in **Fig. 5(c)**, and all kinetics parameters obtained by different models were tabulated in **Table S5**. The linear fitting between q_t and $t_{1/2}$ is multilinear and can be divided into three phases, and K_{d1} is much higher than K_{d2} and K_{d3}, indicating that the first stage corresponds to the instant diffusion stage with the most rapid rate. Notably however, none of the fitted linear portions corresponding to the above three stages pass through the origin. This observation suggests the probable presence of boundary layer or other factors influencing the entire Li^+ adsorption onto the HMO-EtOH & SDS sub-micron spheres, in addition to the intra-particle diffusion. To determine the authentic rate controlling step for the adsorption of Li^+ onto the HMO-EtOH & SDS sub-micron spheres, or to ascertain whether the film diffusion or the pore diffusion had dominated the adsorption, the Boyd model was also deployed for analysis on the adsorption kinetics. As displayed in **Fig. 5(d)**, the straight lines showing linear relation between Bt and t within various ranges for the HMO-EtOH & SDS sub-micron spheres do not pass by the origin, indicating that the pore diffusion and film diffusion jointly control the adsorption rate[23, 37].

3.8 Probable EtOH and SDS co-modified mechanism of the HMOs for efficient enhancement in adsorption of Li^+

Based on the above results, the probable EtOH and SDS co-modified structure and surface of the HMOs sub-micron spheres for efficient enhancement in adsorption of Li^+ ions and corresponding transformation between LMOs and HMOs can be illustrated in **Fig. 6**. As the lithium ion-sieve precursors, the LMOs are converted into the lithium ion-sieves HMOs through acid washing, where H^+ ions within acid solution exchanges with constitutional Li^+ ions of the LMOs crystal skeleton. When exposed in Li^+ -containing solution, H^+ ions within the framework of the lithium ion-sieves HMOs exchange with the Li^+ , thereby achieving the adsorption of Li^+ ions.

Undoubtedly, EtOH and SDS play key roles in the co-modification of the structure and surface of the LMOs and their

corresponding HMOs. When neither EtOH nor SDS exists, LMO-Nothing and relevant HMO-Nothing particles exhibit quasi-spherical or quasi-cubic morphology. The adsorbent HMO-Nothing particles show poor hydrophilicity with an approximate contact angle (CA) of 33.2º and a small specific surface area of 27.84 m^2 g^{-1}, so they exhibit a slower adsorption rate (t_e=9.0 h) and a lower adsorption capacity (q_e=31.52 mg g^{-1}). However, with the addition of SDS, the dispersive LMO-SDS and homologous HMO-SDS particles form micro- and sub-micron spheres with a little wide size distribution. The adsorbent HMO-SDS particles exhibit super-hydrophilicity (CA=0º) and possess a specific surface area of 40.37 m^2 g^{-1}, leading to a faster adsorption rate (t_e=3.0 h) and a clear increase in the adsorption capacity to 41.49 mg g^{-1}. As an anionic surfactant, SDS regulates morphology, promotes spheroidization, and introduces super-hydrophilicity, thus accelerating Li^+ adsorption and increasing the adsorption capacity. Comparatively, when in the presence of EtOH, the remarkable irregular LMO-EtOH and counterpart HMO-EtOH particles bearing sub-micron spherical, column- or nanoplate-like shape have been formed, with somewhat smaller size. The adsorbent HMO-EtOH particles show poor hydrophilic surface (CA=34.1º) and a specific surface area of 60.66 m^2 g^{-1}, resulting in an adsorption equilibrium time of 6.0 h and an adsorption capacity of 47.33 mg g^{-1}. The introduction of EtOH improves the dispersion of the adsorbent. It reduces agglomeration, optimizes the porous structure, and increases the specific surface area to expose more active sites, thus accelerating the adsorption rate and enhancing the adsorption capacity. In contrast, the co-existence of SDS and EtOH gives rise to uniform LMO-EtOH & SDS and corresponding HMO-EtOH & SDS sub-micron spheres, with distinct small diameter and narrow diameter distribution as well as high dispersion. The adsorbent particles exhibit super-hydrophilicity (CA=0º) and a high specific surface area of 120.06 m^2 g^{-1}, bringing about an adsorption equilibrium time of 3.0 h and an adsorption capacity of 56.71 mg g^{-1}. Thus, co-modified structure and surface of the HMO-EtOH & SDS sub-micron spheres by SDS and EtOH have rendered promotion in the spherical morphology, decrease in the diameter of the spheres and increase in the dispersion. Such co-modification with more adsorption sites favors shortening the diffusion path and hence resulting in particularly efficient improvement in adsorption of Li^+.

3.9 Recycling lithium adsorption performance and adsorption selectivity

The equilibrium lithium uptakes of the lithium ion-sieve HMO-Nothing and HMO-EtOH & SDS sub-micron spheres over

five cycles were shown in **Fig. 7(a)**. For each cycle, the adsorption capacity of the HMO-EtOH & SDS sub-micron spheres consistently and conspicuously exceeds that of the HMO-Nothing. During the 5 cycles, the equilibrium lithium uptake of the HMO-EtOH & SDS sub-micron spheres gradually decreases from the top 56.71 mg g^{-1} to the bottom 44.63 mg g^{-1} and then slightly rises to 45.50 mg g^{-1}. For comparison, the equilibrium lithium uptake of the HMO-Nothing descends from the highest 31.56 mg g^{-1} to the lowest 24.41 mg g^{-1} and then ascends a bit to 24.63 mg g^{-1} and finally to 25.25 mg g^{-1}. Combined with **Fig. 7(b)**, the manganese (Mn) dissolution rate of the HMO-EtOH & SDS sub-micron spheres declines from the original 5.25 wt% to 4.93 wt% to 3.65 wt% and to the lowest 3.57 wt% within the first four cycles, which tends to be relatively stable thereafter and ultimately approaches 3.61 wt%. This variation in the Mn dissolution rate corresponds to the changing trend of the equilibrium lithium uptake q_e. To see the changes in the chemical composition and morphology during the recycling adsorption test, the XRD patterns (**Fig. 7(c)**) and SEM images (**Fig. 7(d, e)**) of the HMO-EtOH & SDS sub-micron spheres after the 1st (**Fig. 7(c_1, d)**) and 5th (**Fig. 7(c_2, e)**) cycle were monitored. As can be seen, after 5 cycles of adsorption, a little lower crystallinity HMO-EtOH & SDS sub-micron spheres with rudimental spherical morphology preserved have been emerged, accompanied by some discrete tiny nanocrystals largely owing to the Mn dissolution. Apparently, both the XRD and SEM results indicate the satisfactory stable chemical composition, structure and morphology, which bring about the excellent recycling adsorption performance of the as-obtained HMO-EtOH & SDS sub-micron spheres.

Besides, the adsorption selectivity was also evaluated using the simulated salt lake brine. As convinced in **Fig. 7(f, f_1)**, the highest equilibrium lithium uptake (q_e=25.41 mg g^{-1}) has been acquired for Li^+, conspicuously higher than that of other coexisting metal ions such as Na^+ (4.23 mg g^{-1}), K^+ (1.32 mg g^{-1}), Ca^{2+} (0.85 mg g^{-1}) and Mg^{2+} (6.30 mg g^{-1}) owing to their limited adsorption. Meanwhile, as indicated in **Fig. 7(f_1)**, the separation coefficients (α_M^{Li}) of Li^+ from other metal ions are distinctly impressive. For typical monovalent cations such as Na^+ and K^+, an especially high $\alpha_{Na}^{Li} = 2120.57$ and a high $\alpha_K^{Li} = 781.26$ have been achieved, respectively. Clearly, the present α_{Na}^{Li} is much higher than that (1042.46) for the previous adsorption by the manganese-titanium based composite HMTO (Mn:Ti=1:4) lithium ion-sieve (LIS) nanospheres. Whereas for classical divalent cations such as Ca^{2+} and Mg^{2+}, satisfactory $\alpha_{Ca}^{Li} = 35.34$ and $\alpha_{Mg}^{Li} = 412.33$ have been

individually accomplished. In addition, among the co-existing metal ions, the distribution coefficient (K_d) of Li^+ also provides the overwhelmingly optimum value of 148.44 L g^{-1}. The excellent specific adsorption and separation performance of the spinel-type lithium ion-sieve HMO-EtOH & SDS for Li^+ ions mainly originates from the ion-sieve memory effect. After acid treatment for Li^+ extraction, the material retains a complete spinel framework, whose three-dimensional lattice tunnel size matches well with the ionic radius of Li^+, enabling the reversible intercalation and deintercalation of Li^+ ions inside the crystal lattice[29]. In contrast, the coexisting competing ions in salt lake brine, including Na^+, K^+, Mg^{2+}, Ca^{2+}, possess much larger ionic or hydrated radii than the tunnel size, so they can barely enter the lattice framework and only undergo weak physical adsorption on the material surface[29]. Such precise structural sieving endows the lithium ion-sieve with specific recognition and preferential adsorption toward Li^+, thereby maintaining outstanding separation selectivity even in solutions with high concentrations of competing ions. Both the α_M^{Li} and K_d reconfirm the excellent selective adsorption of Li^+ by the present HMO-EtOH & SDS sub-micron spheres, also demonstrating their great potential practical applications for high efficiency adsorption of Li^+ from high magnesium-lithium molar ratio, especially high potassium-lithium molar ratio salt lake brine.

Fig. 7(g) further vividly presents the adsorption selectivity and cycling process of the HMO-EtOH & SDS sub-micron spheres. Apparently, the HMO-EtOH & SDS sub-micron spheres exhibit high adsorption capacity and remarkable selectivity for Li^+ in simulated salt lake brine[50-52]. H^+ ions of the HMO-EtOH & SDS sub-micron spheres can only be replaced by the adsorbed Li^+ ions with similar radii, leading to LMO-EtOH & SDS which can again turn back to HMO-EtOH & SDS sub-micron spheres by desorption of Li^+ under acid washing. Comparatively, other coexisting metal ions within solution such as Na^+, K^+, Ca^{2+} and Mg^{2+} can only be finitely and physically adsorbed through the surfaces and porous structures of the as-obtained sub-micron spheres.

3.10 Analysis on the XPS spectra of the LMO-EtOH & SDS and HMO-EtOH & SDS

To further investigate the cause of manganese dissolution during cyclic process, XPS analysis was also conducted on the lithium ion-sieve precursor LMO-EtOH & SDS and lithium ion-sieve HMO-EtOH & SDS. As demonstrated in **Fig. 8(a)**, the full-spectra of the LMO-EtOH & SDS (**Fig. 8(a_1)**) and HMO-EtOH & SDS (**Fig. 8(a_1)**) both contain characteristic peaks

of Mn and O, confirming the well preserved and stable framework of the HMO-EtOH & SDS. **Fig. 8(b)** reveals the high-resolution O 1s spectra, the three asymmetric peaks correspond to H_2O, OH^-, and O^2, which may be related to the surface hydrophilicity of the LMO-EtOH & SDS and the HMO-EtOH & SDS[52, 53]. Furthermore, the Mn 2p (**Fig. 8(c)**) and Mn $2p_{3/2}$ (**Fig. 8(d)**) spectra exhibit two Mn 2p peaks ascribed to the spin−orbit splitting. The peaks at binding energy of 643.23 eV and 642.34 eV are assigned to Mn^{4+} and Mn^{3+}, respectively[54], indicating the mixed oxidation state of Mn^{4+} and Mn^{3+} co-existed within the LMO-EtOH & SDS and the HMO-EtOH & SDS. Meanwhile, the corresponding parameters are shown in **Table S6**. Compared with the LMO-EtOH & SDS, the HMO-EtOH & SDS shows a lower Mn^{3+} proportion and a higher average valence. As known, the precursor LMO-EtOH & SDS needs acid washing process to obtain the lithium ion-sieve HMO-EtOH & SDS, during which Mn^{3+} is transformed into Mn^{2+} and Mn^{4+}. The homologous manganese dissolution reaction can be written as the following **eqn. (18)**[55]. Thus, the XPS results clearly manifest the manganese dissolution during the acid washing for HMO-EtOH & SDS.

$$2Mn^{3+} \rightarrow Mn^{2+} + Mn^{4+} \quad (18)$$

3.11 Comparison of the lithium adsorption performances for the HMO-EtOH & SDS and other typical adsorbents in literatures

To objectively evaluate the adsorption performances of the as-synthesized HMO-EtOH & SDS sub-micron spheres, typical adsorbents reported in recent years[14, 17, 22, 23, 26, 28-30, 41] were listed **in Table 2**. Comparatively and noticeably, of the referred adsorbents, the HMO-EtOH & SDS submicron-spheres demonstrate some distinct advantages in the maximum adsorption capacity (q_e=58.74 mg g^{-1}), adsorption equilibrium rate (t_e=3.0 h), specific surface area (120.06 m^2 g^{-1}) and α_{Na}^{Li} (2120.57). Specifically, the present q_m is conspicuously higher than the surface-fluorinated $H_{1.6}Mn_{1.6}O_4$[29], S and Al co-doped $H_{1.6}Mn_{1.6}O_4$[28], Al doped $H_{1.33}Mn_{1.67}O_4$[26], Mg doped $H_{1.6}Mn_{1.6}O_4$[41], Al and Cr co-doped $H_{1.6}Mn_{1.6}O_4$[30], Mo doped $H_4Mn_5O_{12}$[17] and three-dimensional $H_{1.6}Mn_{1.6}O_4$[14], which is however somewhat lower than that of the Deox-$H_{1.6}Mn_{1.6}O_4$[22] and manganese-titanium based composite HMTO nanospheres[23]. The t_e and S_{BET} of the current HMO-EtOH & SDS demonstrate the shortest and highest value, revealing the most rapid adsorption rate and highest specific surface area, respectively. Combined with shortest t_e ,relatively high α_{Mg}^{Li} (412.33), particularly highest

α_{Na}^{Li} (2120.57) and also comparatively satisfactory cyclic performance (q_e of the 5th cycle is 80.23 wt% of that for the 1st cycle, distinctly higher than the HMTO nanospheres[23]) definitely reveal the great potential of the present HMO-EtOH & SDS sub-micron spheres as practical and competitive candidate adsorbents of Li^+ ions from high magnesium to lithium ratio, especially superior sodium to lithium ratio salt lake brines.

For Mn dissolution loss, the Mn dissolution rate of the HMO-EtOH & SDS is 5.25 wt%, which is relatively high among the comparative literature results (**Table 2**). This phenomenon can be mainly attributed to its high specific surface area (S_{BET} =120.06 m^2 g^{-1}), which enables facile exposure of more active sites and porous structures to the acidic elution environment, leading to relatively aggravated Mn dissolution. The modification strategy in this work focuses more on enhancing adsorption capacity and adsorption rate of Li^+ ions, which however can hardly render a reasonable trade-off in Mn dissolution control at present. Notably, despite the relatively high Mn dissolution rate, both the impressive high maximum adsorption capacity and acceptable retention of HMO-EtOH & SDS after 5 cycles (80.23%) suggest the bright future of the HMO-EtOH & SDS as great promising candidate adsorbents for Li^+ ions.

4 Conclusions

In summary, the manganese-based lithium ion-sieve HMO-EtOH & SDS sub-micron spheres were synthesized, employing manganese sulfate monohydrate, lithium hydroxide monohydrate and ammonium bicarbonate as the raw materials, with SDS and EtOH as the additives. For optimization of the synthetic process, the mass ratio of SDS to $MnSO_4 \cdot H_2O$ (50 wt%), volume ratio of EtOH to H_2O (1:3), adsorption pH (pH=12) and adsorption temperature (T=35 ℃) were determined. EtOH can effectively enable the adsorbent particles with smaller average diameter and improved dispersibility, while SDS can render the adsorbent particles with spherical morphology and increased hydrophilicity. When utilized as the adsorbent for Li^+, the HMO-EtOH & SDS sub-micron spheres exhibited an excellent maximum adsorption capacity (q_m=58.74 mg g^{-1}) and fast adsorption rate (t_e=3.0 h), higher and faster than that of most of other typical adsorbents in recent literatures. In addition, the HMO-EtOH & SDS sub-micron spheres also delivered excellent Li^+ exchange capacity (25.41 mg g^{-1}) and high selectivity (α_{Mg}^{Li}=412.33, α_{Na}^{Li}=2120.57) for the adsorption of Li^+ from the simulated salt lake brine. Besides, the HMO-EtOH & SDS sub-micron spheres displayed satisfactory recycling performance, after five cycles of

adsorption-desorption, the adsorption capacity still retained 80.23 wt% of that for the initial adsorption. And for all cycles of adsorption, the manganese leaching ratio remained below 5.25 wt%. Taking the relatively high q_m, short t_e, high α_{Mg}^{Li}, high α_{Na}^{Li}, satisfactory recycling performance, and low manganese leaching ratio into account, the as-obtained HMO-EtOH & SDS sub-micron spheres provide a great potential and competitive candidate adsorbent for Li^+ extraction from simulated and also future probably authentic high Mg/Li ratio, especially high Na/Li ratio salt lake brines. Future work will continuously focus on decreasing Mn dissolution on the basis of the present high capacity and fast adsorption kinetics by means of combining elemental doping, surface coating, design and construction of core-shell structure, etc., and corresponding work is in progress within our group.

Acknowledgements

This work was supported by the Natural Science Foundation of Shandong Province, China (No. ZR2022MB075), State Key Laboratory of Organic-Inorganic Composites, China (oic-202401016), and State Key Laboratory of Chemical Engineering and Low-carbon Technology, China (SKL-ChE-24A02).

References:

[1] Deng, Y.; Chai, G.; Zhang, Y. Research progress on lithium extraction from salt-lake brine. *Journal of Industrial and Engineering Chemistry* **2025**, *148*, 92-108.

[2] Ding, T.; Zheng, M.; Peng, S.; Lin, Y.; Zhang, X.; Li, M. Lithium extraction from salt lakes with different hydrochemical types in the Tibet Plateau. *Geoscience Frontiers* **2023**, *14,* 101485.

[3] Liu, G.; Zhao, Z.; Ghahreman, A. Novel approaches for lithium extraction from salt-lake brines: A review. *Hydrometallurgy* **2019**, *187*, 81-100.

[4] Sharifian, S.; Nikfar, S.; Subasinghe, C.; Iranmanesh, Z.; Rezaee, M.; Vahidi, E. Conventional vs. direct vs. electrochemical lithium extraction: a holistic TEA–LCA of lithium carbonate production from spodumene. *Green Chemistry* **2026**, *28*, 1144-1157.

[5] Wu, H.; Dong, T.; Zhang, Z.; Cheng, Y. Extraction technologies for lithium resources from salt lake brines: research progress, challenges and future prospects. *Metals* **2025**, *15*, 1327.

[6] Yang, M.; Zhong, Y.; Liu, X.; Wang, S.; Qu, T. Review of technologies to extract lithium from hard rock lithium minerals. *Minerals Engineering* **2025**, *232*, 109577.

[7] Opoku, P. A.; Tadesse, B.; Albijanic, B.; Nikoloski, A. N. An overview of coarse particle beneficiation of lithium ores. *Scientific Reports* **2025**, *15*, 29091.

[8] Alghamdi, M.; Altmann, T.; Das, R. Direct lithium extraction from seawater brine: an assessment of technology and existing commercial systems. *Minerals* **2025**, *15*, 512.

[9] Peng, C.; Zhai, C.; Liu, Y.; He, L.; Liu, X. Direct lithium extraction from α-spodumene ore via alkali leaching-Li/Al co-precipitation method. *Separation and Purification Technology* **2025**, *370*, 133199.

[10] Shi, X.; Zhang, Q.; Wang, Z.; Bi, Q.; Lin, Y. Acetone-modulated reverse interfacial polymerization was employed to prepare PEI/PDA positively charged composite nanofiltration membranes for Mg^{2+}/Li^+ separation. *Journal of*

Membrane Science **2025**, *720*, 123780.

[11] Guo, L.; Yao, Y.; Xu, J.; Ang, E. H.; Xu, G.; Liao, J.; Sotto, A.; Shen, J. Strategies for lithium extraction from salt lakes by nanofiltration and selective-electrodialysis and analysis of differences between the two methods. *Desalination* **2024**, *586*, 117749.

[12] Lu, Q.; Liu, P.; Zhou, T.; Huang, R.; Zhang, K.; Hu, L.; Liu, R.; Ren, Z.; Wang, J.; Wang, X. Recent progress on electro-sorption technology for lithium recovery from aqueous sources. *Nano Research* **2023**, *17*, 2563-2573.

[13] Gao, Y.; Zhang, H.; Lei, P.; Sun, X. A deep eutectic solvent extraction strategy based on primary ammonium and β-diketone for separating Li from high Na/Li brine. *Desalination* **2025**, *614*, 119123.

[14] Li, X.; Tao, B.; Jia, Q.; Guo, R. Preparation and adsorption performance of multi-morphology H1.6Mn1.6O4 for lithium extraction. *Chinese Journal of Chemical Engineering* **2021**, *34*, 68-76.

[15] Liu, P.; Yan, X.; Chen, Z.; Qin, Y.; Yang, L.; Ma, J. Preparation of half-coated manganese oxide lithium ion-sieve precursor with low manganese dissolution loss for lithium recovery. *Journal of Water Process Engineering* **2025**, *74*, 107785.

[16] Wang, Q.; Yang, X.; Li, C.; Zhao, C.; Huang, Y.; Qiu, S.; Qin, Y.; Shi, C. Titanium-based lithium ion sieve adsorbent H_2TiO_3 with enhanced Li^+ adsorption properties by magnetic Fe doping. *Separation and Purification Technology* **2024**, *346*, 127455.

[17] Wu, H.; Yan, G.; Liu, X.; Yang, G. Molybdenum-doped manganese-based ion sieves for enhanced liquid lithium extraction performance. *Journal of Environmental Chemical Engineering* **2025**, *13*, 116229.

[18] Cao, Y.; Chen, J.; Lin, S.; Yu, J. Granulating-avoiding aluminum-based adsorbents for fast salt lake lithium extraction with low freshwater consumption. *Chemical Engineering Journal* **2025**, *523*, 168234.

[19] Zhang, L.; Zhang, T.; Zhao, Y.; Dong, G.; Lv, S.; Ma, S.; Song, S.; Quintana, M. Doping engineering of lithium-aluminum layered double hydroxides for high-efficiency lithium extraction from salt lake brines. *Nano Research* **2023**, *17*, 1646-1654.

[20] Gok, X. Y.; Lau, H. S.; Liang, C. Z.; Yong, W. F. Titanium-based lithium-ion sieves granulated with biomaterial for sustainable lithium recovery. *Results in Engineering* **2025**, *26*, 105269.

[21] Zeng, Z.; Peng, Z.; Wang, Y.; Liu, G.; Zhou, Q.; Qi, T.; Shen, L. Synthesis of Fe-doped lithium-ion sieve and its application on lithium adsorption in sodium aluminate solution. *Jom* **2025**, 10.1007/s11837-025-07966-z.

[22] Bao, L.-R.; Tang, W.-P.; Sun, S.-Y. Semi-wet synthesis of high-performance $Li_{1.6}Mn_{1.6}O_4$ for selective lithium extraction from Salt Lakes Brine. *Desalination* **2024**, *584*, 117730.

[23] Wang, Y.; Liu, Z.-Y.; Su, Y.; Liu, Y.; Liu, A.; Zhang, X.; Huang, Y.; Zhang, L.; Chen, H.; Zhu, W. Uncovering fantastic synergistic lithium adsorption with manganese-titanium based composite nanospheres: Mild synthesis and molecular dynamics simulation insights. *Journal of Energy Chemistry* **2025**, *101*, 52-67.

[24] Weng, D.; Duan, H.; Hou, Y.; Huo, J.; Chen, L.; Zhang, F.; Wang, J. Introduction of manganese based lithium-ion Sieve-A review. *Progress in Natural Science: Materials International* **2020**, *30*, 139-152.

[25] Yang, P.; Hai, C.; Sun, Y.; Dong, S.; He, X.; Xu, Q.; Ma, L.; Zhou, Y. Accelerating adsorption capacity and structural stability of $Li_{1.6}Mn_{1.6}O_4$-type adsorbents via synergetic effect of in-situ configured Li_2MnO_3 layer. *Chemical Engineering Journal* **2024**, *495*, 153330.

[26] Li, X.; Li, X.; Chen, G.; Zhang, D.; Tian, L.; Chen, J.; Liu, C.; Li, B.; Tiraferri, A.; Liu, B. Efficient recovery of lithium from shale gas wastewater: Fe, Ni, and Al doping of $H_{1.33}Mn_{1.67}O_4$ for improved adsorption capacity and manganese loss reduction. *Journal of Cleaner Production* **2024**, *473*, 143554.

[27] Li, Z.; Li, W.; Song, X.; Zhu, Y.; Ding, X.; Zhao, Y.; Li, L.; Zhang, L.; Liu, M.; Zhu, C.; Chen, Z.; Wang, S. Study of the influence of doping and coating modification methods on Mn dissolution loss in lithium ion-sieves via density functional theory and molecular dynamics simulations. *Surfaces and Interfaces* **2025**, *74*, 107652.

[28] Su, Y.; Qian, F.; Qian, Z. Enhancing adsorption capacity and structural stability of $Li_{1.6}Mn_{1.6}O_4$ adsorbents by anion/cation co-doping. *RSC Advances* **2022**, *12*, 2150-2159.

[29] Zhang, G.; Zhang, J.; Zeng, J.; Sun, Y.; Shen, Y.; Li, X.; Ren, X.; Hai, C.; Zhou, Y.; Tang, W. Improved structural stability and adsorption capacity of adsorbent material $Li_{1.6}Mn_{1.6}O_4$ via facile surface fluorination. *Colloids and Surfaces A: Physicochemical and Engineering Aspects* **2021**, *629*, 127645.

[30] Gao, Y.; Wang, S.; Gao, F.; Guo, C.; Dong, J.; Chen, G. Al and Cr ions co-doped spinel manganese lithium

ion-sieve with enhanced Li^+ adsorption performance and structural stability. *Microporous and Mesoporous Materials* **2023**, *351*, 112492.

[31] Zhang, G.; Wei, Q.; Xia, X.; Huang, D.; Tang, W.; Yu, W. W. Synergistic doping and coating of lithium ion-sieves for enhanced lithium recovery from brine. *Desalination* **2025**, *601*, 118556.

[32] Han, X.; Wang, H.; Sun, C.; Xue, H. External‐Field‐Driven Functional Nanomaterials for Interdisciplinary Engineering-Medicine Applications. *SmartMat* **2025**, *6*, e70053.

[33] Li, W.; Wang, E.; Wang, H.; Yang, Y.; Hu, S.; Liu, H. Construction of S-scheme heterostructure via anion and cation vacancy mediated electrostatically driven self-assembly in $Cd_{1-x}S$-CdS_{1-x} for robust photocatalytic CO_2 reduction. *Nano Energy* **2025**, *142*, 111235.

[34] Song, Y.; Zhao, H.; Lu, W.; Wang, H. Unlocking hydrogen transfer pathway in electrocatalytic CO_2 reduction: Paving the way for precise selectivity control. *Nano Research* **2025**, *18*, 94907384.

[35] Zhao, H.; Wang, J.; Song, Y.; Sun, D.; Zhang, Q.; Lu, W.; Wang, H. Multi-shell Au@Rh nanoantenna reactor with collective plasmonic excitation for photothermal CO_2 methanation. *Nano Research* **2026**, *19*, 94908174.

[36] Hui, Q.; Diao, Y.; Li, Z.; Wang, F.; Guan, Z.; Wang, C.; Zhang, L.; Zhu, W. Organic–inorganic mixed matrix membrane constructed by chitosan and red mud based γ-AlOOH hierarchical porous microspheres as superior adsorbents for anionic dye and microplastics. *Separation and Purification Technology* **2025**, *371*, 133245.

[37] Wang, L.; Li, H.; Li, M.; Zhang, L.; Zhang, H.; Liu, Z.-Y.; Zhu, W. Trace nitrogen-doped hierarchical porous biochar nanospheres: Waste corn roots derived superior adsorbents for high concentration single and mixed organic dyes removal. *Nano Research* **2022**, *16*, 1846-1858.

[38] Zheng, Y.; Wang, L.; Zhang, L.; Zhang, H.; Zhu, W. One-pot hydrothermal synthesis of hierarchical porous manganese silicate microspheres as excellent Fenton-like catalysts for organic dyes degradation. *Nano Research* **2021**, *15*, 2977-2986.

[39] Hui, Q.; Hang, Y.; Wang, F.; Zhang, H.; Zhang, L.; Zhu, W. Rotating hydrothermal route to red mud derived uniform hierarchical porous flowerlike boehmite (γ-AlOOH) microspheres: Force analysis on formation mechanism and superior adsorption performances for anionic dyes removal. *Particuology* **2024**, *94*, 229-244.

[40] Qin, Y.; Yang, X.; Zeng, L.; Dong, J.; Bi, Q.; Wang, Q.; Qiu, S.; Xu, J.; Zhang, Q.; Shi, C. Hydrophilic surface-modified titanium-based lithium ion sieve adsorbents for efficient lithium extraction. *Journal of Molecular Liquids* **2024**, *412*, 125896.

[41] Bao, L.; Zhang, J.; Wu, J.; Zhang, G.; Yang, Y.; Tang, W.; Xue, M. Preparation of Mg-doped $Li_{1.6}Mn_{1.6}O_4$ with enhanced Li^+ adsorption performance and anti-dissolution properties of Mn. *Hydrometallurgy* **2022**, *209*, 105772.

[42] Wang, Y.; Shi, D.; Cao, Y.; Han, X.; Zhang, T.; Zhong, K.; Zhao, Q.; Xu, N.; Bian, S. La3+ doped $H_{1.6}Mn_{1.6}O_4$ lithium-ion sieve for Li^+ efficient adsorption and analysing anti-dissolution loss mechanism. *Particuology* **2025**, *106*, 201-212.

[43] Xie, S.; Yuan, M.; Wang, T.; Liu, J.; Yan, J.; Li, Z.; Peng, J. Sodium dodecyl sulfate (SDS)-assisted preparation of homogeneous monodisperse $MnCO_3$ microspheres and its application to the synthesis of $LiMn_2O_4$. *Ceramics International* **2022**, *48*, 10113-10119.

[44] Yao, Y.; Zhang, L.; Qiu, Y.; Li, Z.; Ma, Z.; Wang, S. Phase–activity relationship of MnO_2 nanomaterials in periodate oxidation for organic pollutant degradation. *Water Research* **2024**, *264*, 122224.

[45] Zhang, Q.-H.; Li, S.-P.; Sun, S.-Y.; Yin, X.-S.; Yu, J.-G. $LiMn_2O_4$ spinel direct synthesis and lithium ion selective adsorption. *Chemical Engineering Science* **2010**, *65*, 169-173.

[46] Ryu, J. C.; Shin, J.; Lim, C.; Kim, K. H.; Ryu, T.; Lee, Y.-S. Lithium ion adsorption characteristics of porous $Li_{1.33}Mn_{1.67}O_4$ adsorbent prepared using petroleum-based pitch as a binder. *Hydrometallurgy* **2022**, *209*, 105837.

[47] Liu, Q.; Zhang, L.; Liu, Y.; Zheng, X.; Liu, X.; Zhong, Z.; Wei, L.; Zhao, Q.; Yao, T.; Yang, P. Preparation, adsorption and structure of Ce doped layered manganese ion-sieve based on Li_2MnO_3 spatial structure. *Environmental Research* **2025**, *273*, 121241.

[48] Gao, A.; Hou, X.; Sun, Z.; Li, S.; Li, H.; Zhang, J. Lithium-desorption mechanism in $LiMn_2O_4$, $Li_{1.33}Mn_{1.67}O_4$, and $Li_{1.6}Mn_{1.6}O_4$ according to precisely controlled acid treatment and density functional theory calculations. *Journal of*

Materials Chemistry A **2019**, *7*, 20878-20890.

[49] Bao, L.-R.; Zhang, J.-Z.; Tang, W.-P.; Sun, S.-Y. Synthesis and adsorption properties of metal oxide-coated lithium ion-sieve from salt lake brine. *Desalination* **2023**, *546*, 116196.

[50] Disu, B.; Rafati, R.; Sharifi Haddad, A.; Muirhead, D. Maximizing Lithium Adsorption and Selectivity on Manganese-Based Ion Sieves: Effects of Thermal Treatment, Acid Content, and Operating Conditions. *Industrial & Engineering Chemistry Research* **2025**, *64*, 11961-11980.

[51] Luo, J.; Shu, J.; Zhao, H.; Wang, J.; Chen, S.; Yang, H.; Lin, F.; Zhang, S.; Chen, M.; Yang, Y. Synthesis of lithium-ion sieves based on electrolytic manganese anode slime: Characterization and its lithium adsorption performance. *Chemical Engineering Journal* **2025**, *523*, 168001.

[52] Tu, Y.; Zhou, Z.; Wei, W.; Guan, L.; Liu, Y.; Xu, Z.; Liu, H.; Liu, Z. Ti surface-doped spinel lithium manganese oxide with porous structure and improved stability for Li extraction from salt-lake brine. *Chemical Engineering Journal* **2025**, *503*.

[53] Li, C.; Li, W.; Chen, K.; Ogunbiyi, A. T.; Zhou, Z.; Duan, Q.; Xue, F. Highly active Pd catalysts supported on surface-modified cobalt-nickel mixed oxides for low temperature oxidation of lean methane. *Fuel* **2020**, *279*, 118372.

[54] Qian, F.; Zhao, B.; Guo, M.; Qian, Z.; Wu, Z.; Liu, Z. Trace doping by fluoride and sulfur to enhance adsorption capacity of manganese oxides for lithium recovery. *Materials & Design* **2020**, *194*, 108876.

[55] Orooji, Y.; Nezafat, Z.; Nasrollahzadeh, M.; Shafiei, N.; Afsari, M.; Pakzad, K.; Razmjou, A. Recent advances in nanomaterial development for lithium ion-sieving technologies. *Desalination* **2022**, *529*, 115624.

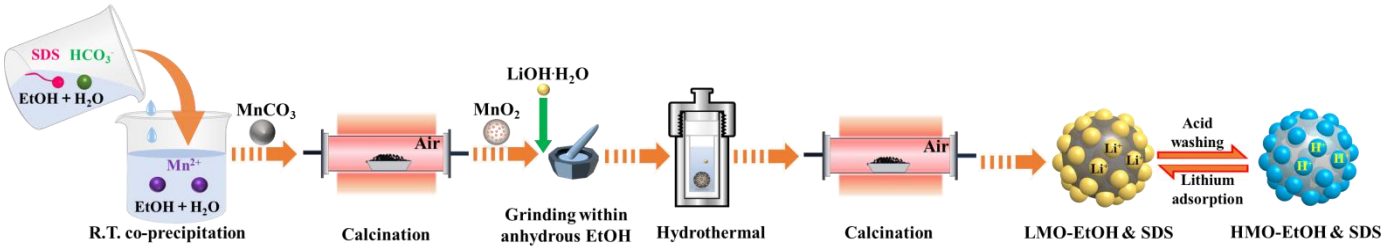

Scheme 1. Illustration of the synthetic procedure for the structure and surface co-modified lithium ion-sieve HMO-EtOH & SDS.

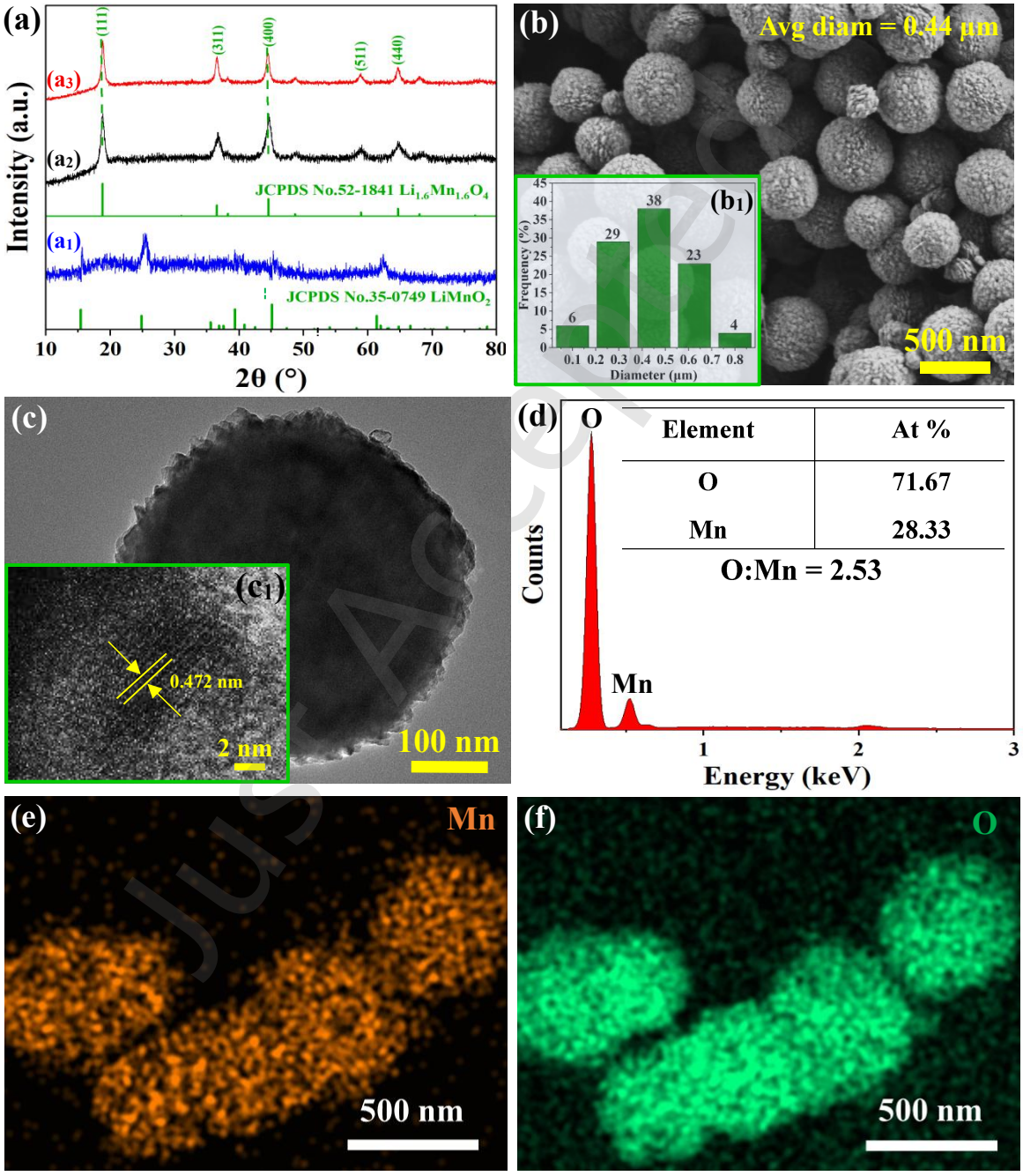

Fig. 1. XRD patterns (a), SEM (b) and TEM (c) images, EDS spectrum (d), Mn (e) and O (f) elemental mappings of the hydrothermal product $LiMnO_2$ (a_1), lithium ion-sieve precursor LMO-EtOH & SDS microspheres (a_2) and lithium ion-sieve HMO-EtOH & SDS microspheres (a_3, b-f). The inset (b_1) and (c_1) show their corresponding diameter distribution and HRTEM image, respectively. Mass ratio of SDS to $MnSO_4·H_2O$= 50 wt%, volume ratio of EtOH to H_2O= 1:3.

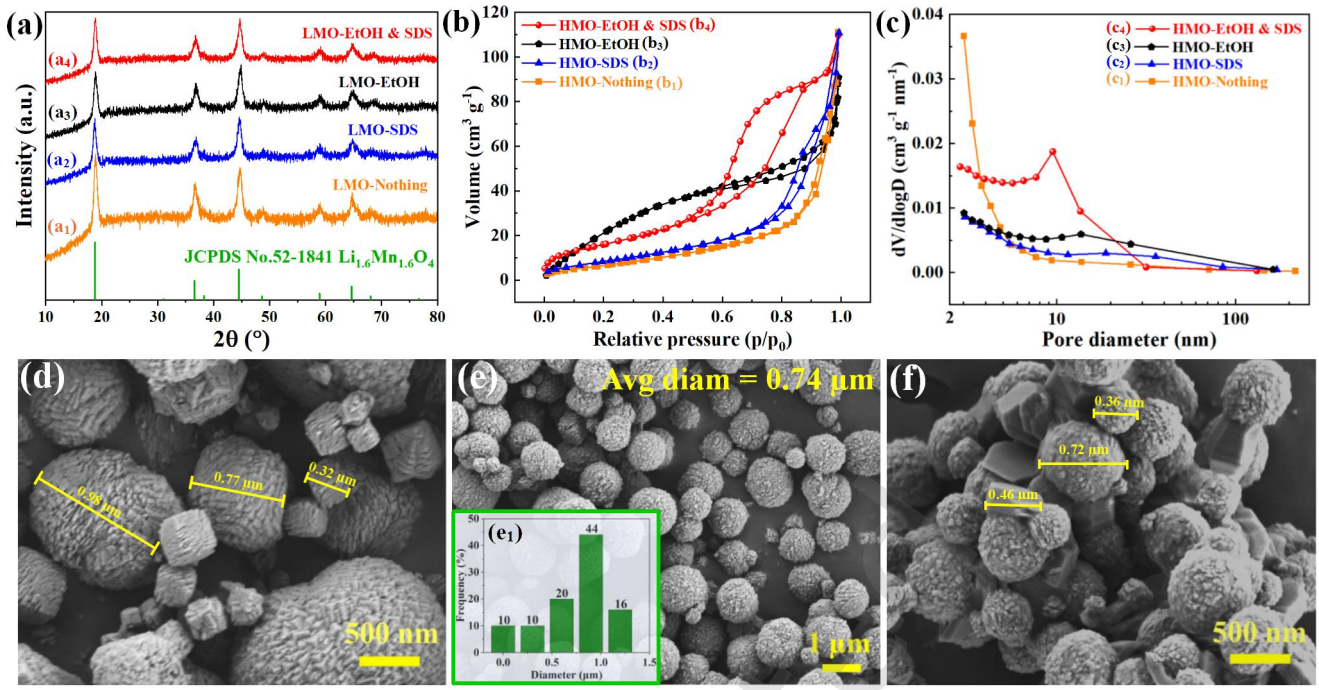

Fig. 2. XRD patterns (a) of the lithium ion-sieve precursors LMO-Nothing (a_1), LMO-EtOH (a_2), LMO-SDS (a_3) and LMO-EtOH & SDS (a_4); Nitrogen adsorption/desorption isotherms (b), pore size distribution (PSD) (c) and SEM images (d-f) of the lithium ion-sieves HMO-Nothing (b_1, c_1, d), HMO-SDS (b_2, c_2, e), HMO-EtOH (b_3, c_3, f) and HMO-EtOH & SDS (b_4, c_4). The inset (e_1) shows the corresponding particle size distribution of the HMO-SDS.

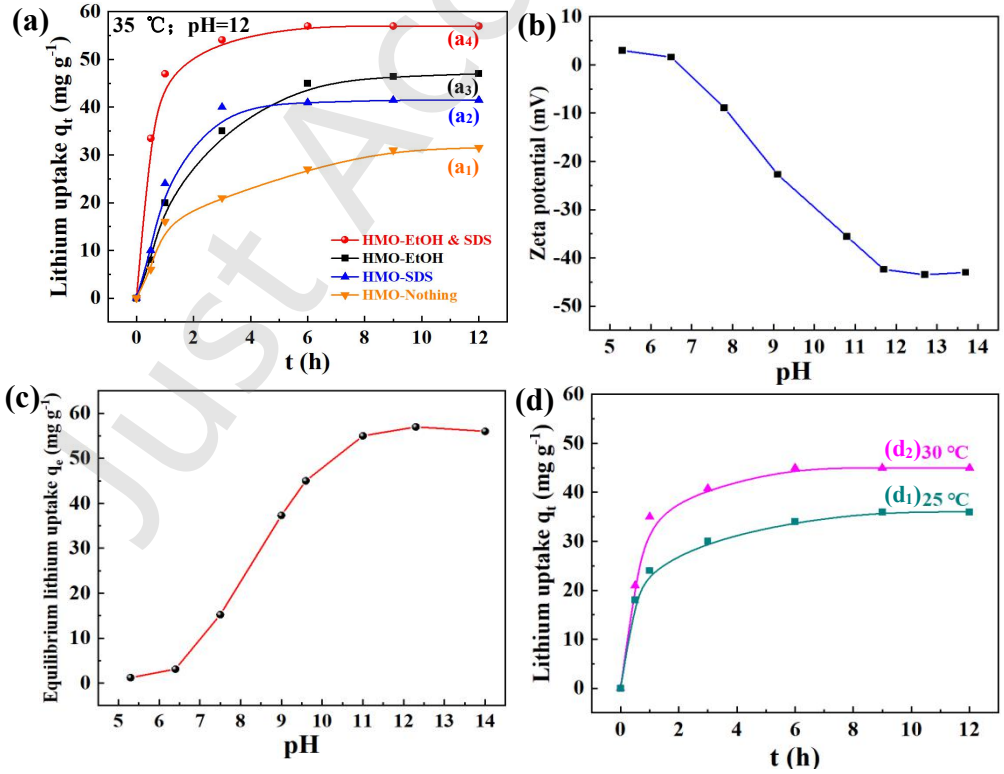

Fig. 3. Variation in the lithium uptake q_t (a) with time for the lithium ion-sieves HMO-Nothing (a_1), HMO-SDS (a_2), HMO-EtOH (a_3) and HMO-EtOH & SDS (a_4), Temperature (℃): 35; pH=12. Variation in the zeta potential (b) and equilibrium lithium uptake q_e (c) of the lithium ion-sieve HMO-EtOH & SDS with pH value at 35 ℃, and corresponding change in the lithium uptake q_t (d) with time at 25 ℃ (d_1), 30 ℃ (d_2) with the initial pH value of 12.

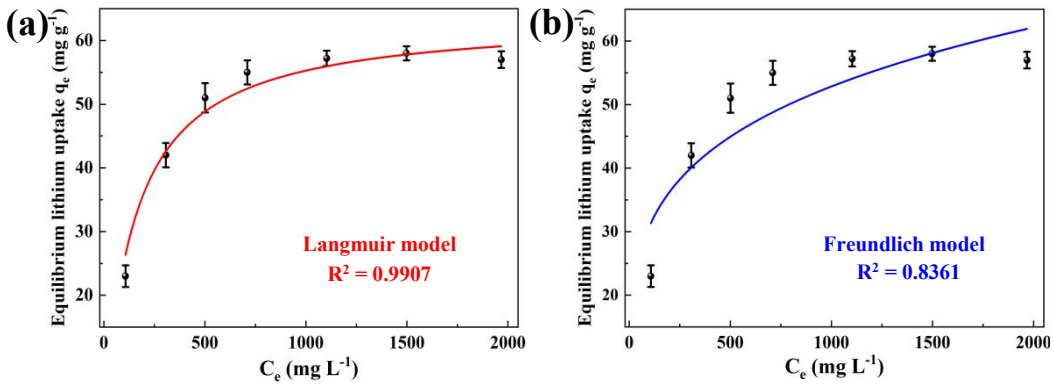

Fig. 4. Adsorption of Li^+ ions on the lithium ion-sieve HMO-EtOH & SDS fitted by non-linear regression with the Langmuir (a) and Freundlich (b) isotherm models. Temperature (ºC): 35; pH=12.

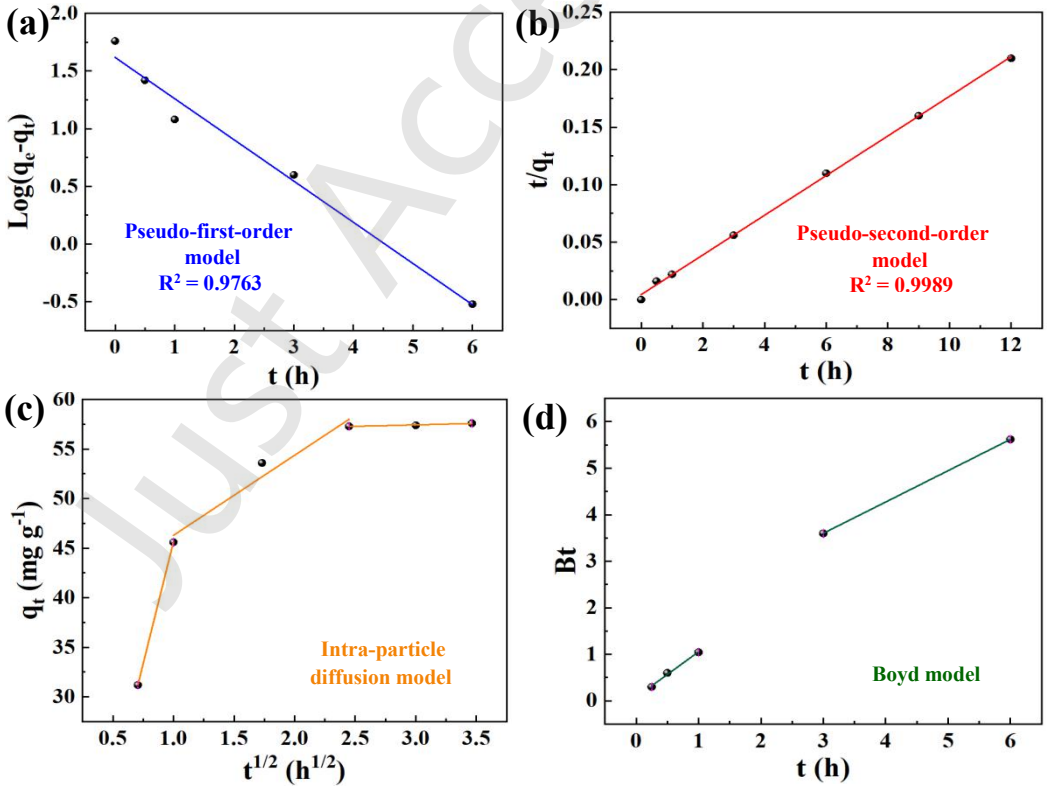

Fig. 5. Pseudo-first-order (a) and pseudo-second-order (b) kinetic models, intra-particle diffusion (c) and Boyd (d) models employed for the lithium adsorption on the lithium ion-sieve HMO-EtOH & SDS, originated from the linear regression, with an initial concentration and dosage of the Li^+ solution as 1.8 g L^{-1} and 100.0 mL, respectively. Temperature (ºC): 35; pH=12.

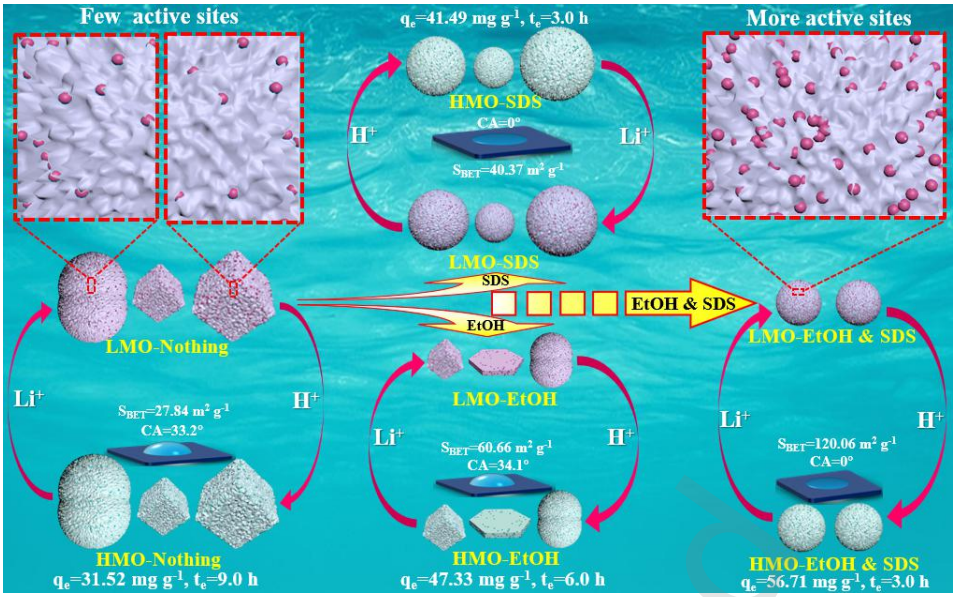

Fig. 6. Probable EtOH and SDS co-modified structure and surface of the HMO-EtOH & SDS sub-micron spheres for efficient enhancement in adsorption of Li^+ ions, as well as the transformation between LMOs and HMOs.

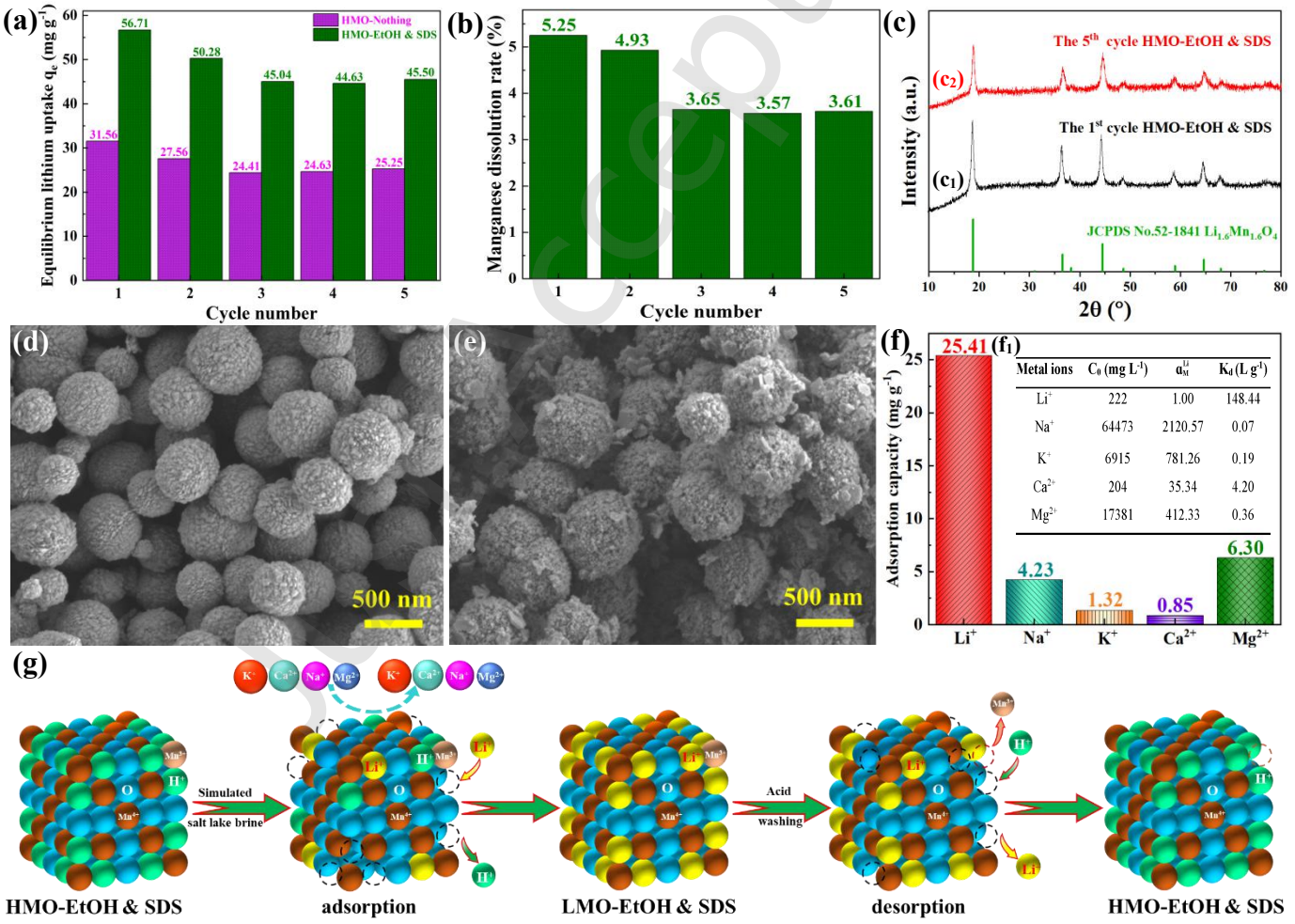

Fig. 7. Variations of the equilibrium lithium uptake q_e during the five cycles of lithium adsorption and desorption on the lithium ion-sieve HMO-Nothing and HMO-EtOH & SDS (a); Variations in the dissolution rate of Mn^{2+} during the five cycles of lithium adsorption and desorption on HMO-EtOH & SDS (b), XRD patterns (c) and SEM images (d, e) of the first (c_1, d) and fifth (c_2, e) cycle, adsorption capacity of different coexisting ions (f) and corresponding parameters (f_1) for the lithium adsorption from the simulated salt lake brine on the lithium ion-sieve HMO-EtOH & SDS, and the corresponding schematic illustration on the adsorption selectivity and cycling process (g). Temperature (ºC): 35; pH=8.5.

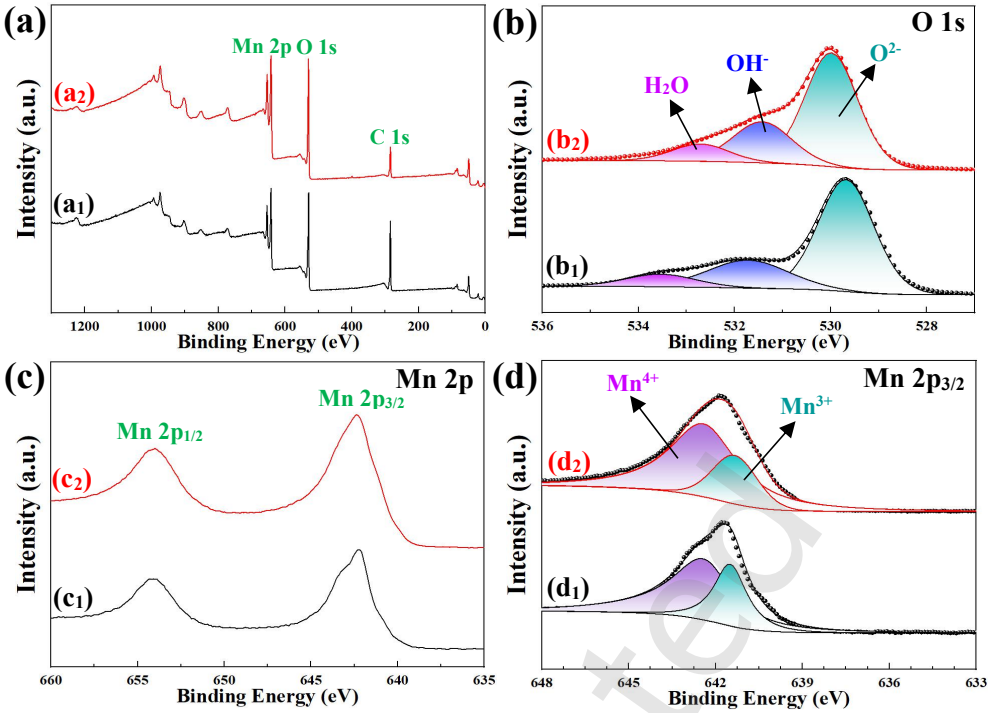

Fig. 8. XPS full spectra (a), O 1s (b), Mn 2p (c) and Mn 2p3/2 (d) high-resolution spectra of the lithium ion-sieve precursor LMO-EtOH & SDS (a_1, b_1, c_1, d_1) and lithium ion-sieve HMO-EtOH & SDS (a_2, b_2, c_2, d_2).

Table 1. The fitting results of the Langmuir and Freundlich isotherm models employed for the Li^+ ions adsorption onto the lithium ion-sieve HMO-EtOH & SDS.

T	Langmuir			Freundlich		
(℃)	q_m (mg·g^{-1})	b (L mg^{-1})	R^2	k_f (L g^{-1})	1/n	R^2
35	58.74	0.0410	0.9907	6.4748	0.2991	0.8361

Table 2. Comparison of the lithium adsorption performances for the HMO-EtOH & SDS and other typical adsorbents recently reported in literatures.

Samples	q_m (mg g^{-1})	t_e (h)	S_{BET} (m^2 g^{-1})	α_{Mg}^{Li}	α_{Na}^{Li}	Cyclic performance	Dissolution loss of Mn (wt%)	Ref.
Surface-fluorinated $H_{1.6}$ $Mn_{1.6}$ O_4	34.00	10.0	10.72	/	/	q_e of the 5th cycle is 91.29% of that for the 1st cycle	1.58	[29]
S and Al co-doped $H_{1.6}$ $Mn_{1.6}$ O_4	41.08	48.0	/	182.05	3398.33	q_e of the 5th cycle is 93.00% of that for the 1st cycle	3.00	[28]
Al doped $H_{1.33}Mn_{1.67}O_4$	39.90	24.0	28.86	237.00	74.30	q_e of the 4th cycle is 90.78% of that for the 1st cycle	1.50	[26]
Mg doped $H_{1.6}Mn_{1.6}O_4$	43.80	>3.0	/	452.00	385.00	q_e of the 10th cycle is 60.00% of that for the 1st cycle	3.23	[41]
Al and Cr co-doped $H_{1.6}Mn_{1.6}O_4$	50.51	> 30.0	63.00	1441.60	256.18	q_e of the 10th cycle is 82.00% of that for the 1st cycle	4.80	[30]
Mo doped $H_4Mn_5O_{12}$	51.20	24.0	/	19511.79	636.20	q_e of the10th cycle is 80.73% of that for the 1st cycle	2.63	[17]
Three-dimensional $H_{1.6}Mn_{1.6}O_4$	55.01	> 6	104.82	395.42	951.66	q_e of the 5th cycle is 74.00% of that for the 1st cycle	3.50	[14]
HMO-EtOH & SDS	58.74	3.0	120.06	412.33	2120.57	q_e of the 5th cycle is 80.23% of that for the 1st cycle	5.25	This work
Deox-$H_{1.6}Mn_{1.6}O_4$	65.21	> 8.0	/	863.63	2035.71	q_e of the 10th cycle is 96.79% of that for the 1st cycle	1.28	[22]
HMTO	87.26	6.0	43.58	2192.76	1042.46	q_e of the 5th cycle is 74.42% of that for the 1st cycle	3.75	[23]

Electronic Supplementary Material

Structure and surface co-modified lithium ion-sieve $H_{1.6}Mn_{1.6}O_4$ sub-micron spheres with efficient enhancement in adsorption of lithium from simulated salt lake brine

Aoqun Liu, Shenbo Zhu, Yueyu Ma, Fanli Meng, Quan Zhou, Yuchen Xue, Yinghao Zhao, Xingguang Zhao, and Wancheng Zhu*
Department of Chemical Engineering, Qufu Normal University, Qufu 273165, China

*Address correspondence to zhuwancheng@tsinghua.org.cn

Supporting information to https://doi.org/10.26599/NR.2026.94908753

Text S1. Materials and reagents

HCl, $NH_3{\cdot}H_2O$ solution and KCl, NaCl, $MgCl_2{\cdot}6H_2O$, $CaCl_2$ were purchased from the Sinopharm Chemical Reagent Co., Ltd. $LiOH{\cdot}H_2O$, $LiCl{\cdot}H_2O$ were bought from the Shanghai Macklin Biochemical Co., Ltd. Sodium dodecyl sulfate (SDS) and NH_4HCO_3 were obtained from the Shanghai Aladdin Biochemical Technology Co., Ltd. $MnSO_4{\cdot}H_2O$ and Li_2CO_3 were got from the Damao Chemical Reagent Co., Ltd. In particular, all chemical reagents were of analytical grade and used without further purification.

Text S2. Influence of pH on the equilibrium adsorption capacity

A lithium-containing solution was first prepared from $LiCl{\cdot}H_2O$, and then its pH was adjusted using a mixture of NH_4 Cl and $NH_3.H_2O$ to achieve the following levels: 5.3, 6.4, 7.5, 9.0, 9.6, 11.0, 12.3, and 14.0. The lithium ion sieve HMO-EtOH & SDS was added to the above lithium-containing solutions with various pH values. The solutions were constantly and magnetically stirred at 35 ºC for 12.0 h, then the equilibrium adsorption capacity q_e of the lithium-ion sieve under each pH value was calculated using **eqn (1)**.

Text S3. Effect of temperature on the adsorption capacity

Effect of temperature on the adsorption capacity was investigated at lithium-containing solution with various temperature. Specifically, HMOs were immersed in three lithium-containing solutions, whose temperatures were preset to 25 ºC, 30 ºC, and 35 ºC, respectively.

The solutions were magnetically stirred for 12.0 h, and at different time intervals, the supernatant was sampled to measure the concentration of Li^+ ions, and then the adsorption capacity q_t of the lithium-ion sieve was calculated using **eqn (2)**. The experimental data were further analyzed using the pseudo-second-order (PSO) kinetic model to derive kinetic parameters at various temperatures.

Text S4. Characterization

X-ray diffraction (XRD) patterns were obtained using an X-ray powder diffractometer (MiniFlex600, Rigaku, Japan) equipped with a Cu-Kα radiation source (λ=1.5406 Å) and operated at a fixed power source (30.0 kV, 10.0 mA), so as to identify the crystal phase of the synthesized product. Images were captured to investigate the morphology and microstructures of the samples, by using a Field emission scanning electron microscopy (SEM, JSM 7401F, JEOL, Japan) and high-resolution transmission electron microscopy (HRTEM, JEM-2010, JEOL, Japan) operated at 3.0 kV and 120.0 kV, respectively. Approximately, 100 particles were directly and randomly selected from typical SEM images to measure and estimate the size distribution of the samples. Nitrogen adsorption-desorption isotherms were recorded using a physisorption profiler (Kubo X1000, Beijing Builder Electronic Technology Co., Ltd.) at 77 K to determine the porous structure within the samples. Prior to this, the samples had been deaerated at 150°C for 3.0 h. Specific surface area (SSA) was calculated using the multipoint Brunauer-Emmett-Teller (BET) method from the adsorption branches within the relative pressure (p/p_0) range of 0.2-1.0. The pore size distribution (PSD) was assessed using the Barrett-Joyner-Halenda (BJH) model from the nitrogen desorption isotherm. For determination of the elements on the surface, an X-ray photoelectron spectroscopy (XPS, Thermo K-alpha, USA) was applied. The concentrations of Li^+ ions in the solutions were determined using an atomic absorption spectrophotometer (AAS, TAS-990F, Beijing Purkinje General Instrument Co., Ltd.) at a detection wavelength of 670.8 nm. The concentrations of other ions in the solution, including Na^+, K^+, Ca^{2+}, Mg^{2+} and Mn^{2+}, were determined using an inductively coupled plasma optical emission spectrometry (ICP-OES, Agilent 5110, Agilent Technologies Co., Ltd.).

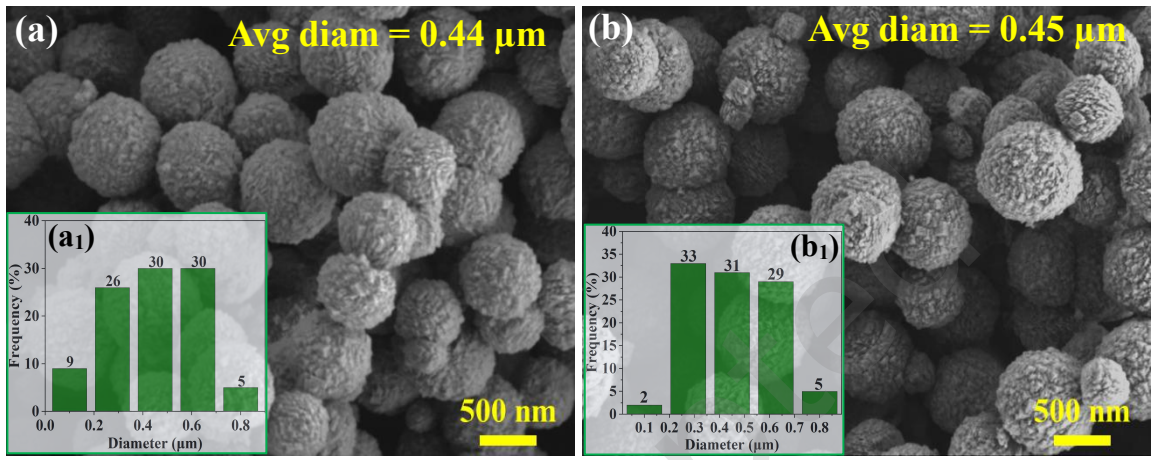

Fig. S1. SEM images of the hydrothermal product $LiMnO_2$ (a) and lithium ion-sieve precursor LMO-EtOH & SDS (b), with the inset (a_1) and (b_1) showing their corresponding diameter distribution.

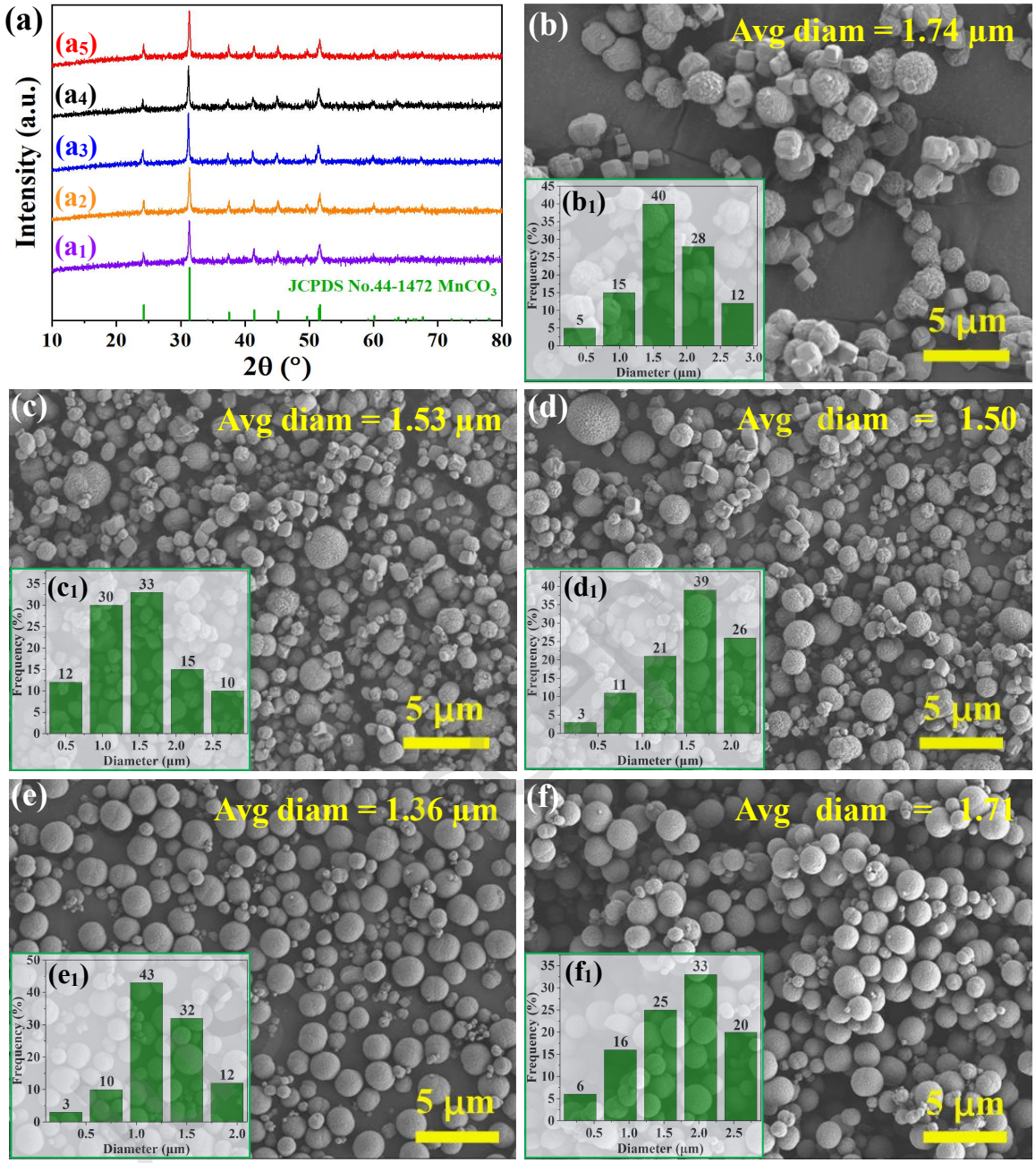

Fig. S2. XRD patterns (a) and SEM images (b-f) of the $MnCO_3$ submicron-spheres synthesized with various mass ratio of SDS to $MnSO_4 \cdot H_2O$ as 0 (a_1, b), 30 wt% (a_2, c), 40 wt% (a_3, d), 50 wt% (a_4, e), and 60 wt% (a_5, f). The insets (b_1-f_1) indicate their corresponding diameter distributions, respectively.

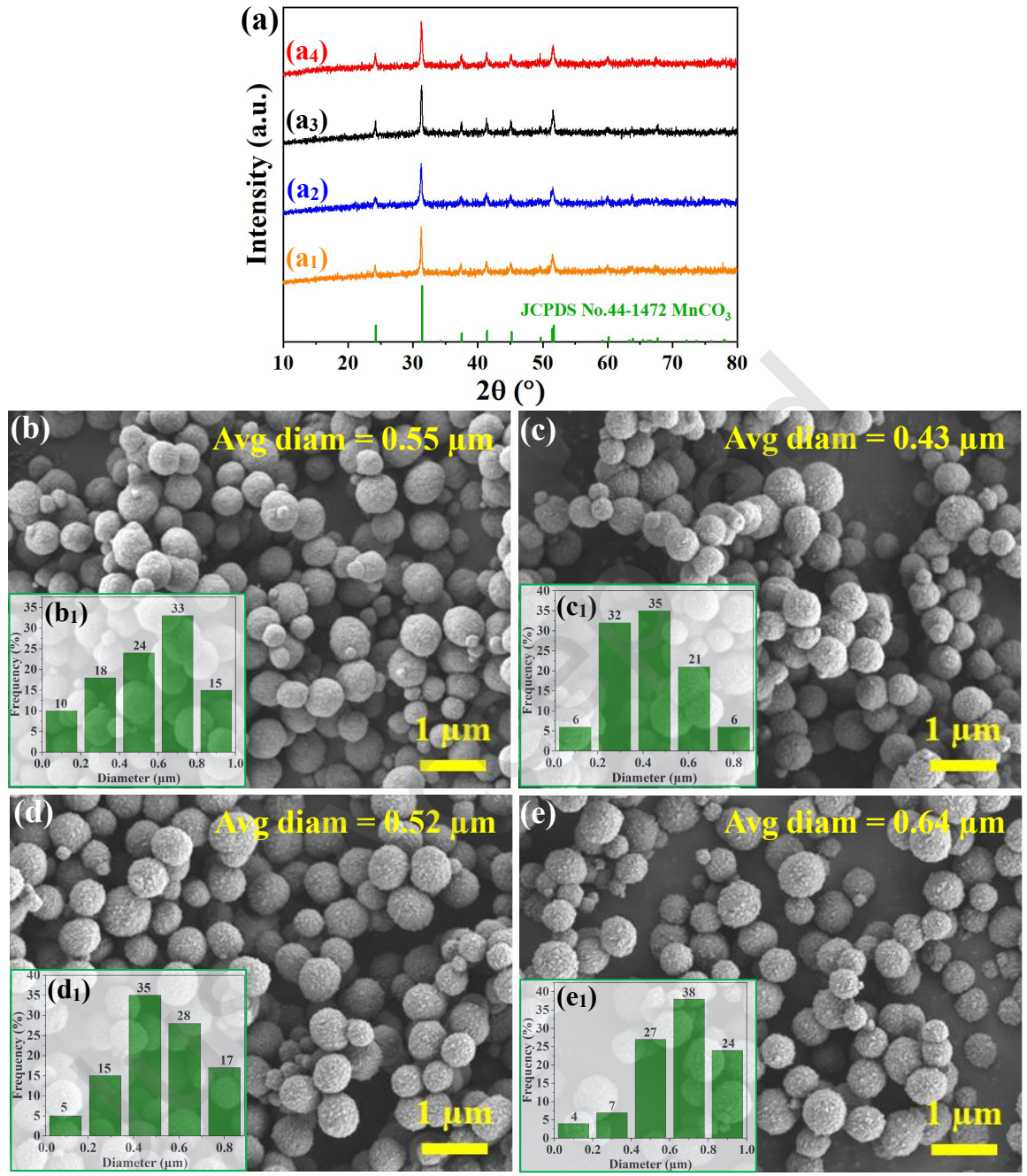

Fig. S3. XRD patterns (a) and SEM images (b-e) of the $MnCO_3$ submicron-spheres synthesized with different volume ratios of EtOH to H_2O as 1:4 (a_1, b), 1:3 (a_2, c), 1:2 (a_3, d) and 1:1 (a_4, e), in the presence of mass ratio of SDS to $MnSO_4 \cdot H_2O$ as 50 wt%. The insets (b_1-e_1) indicate their corresponding diameter distributions, respectively.

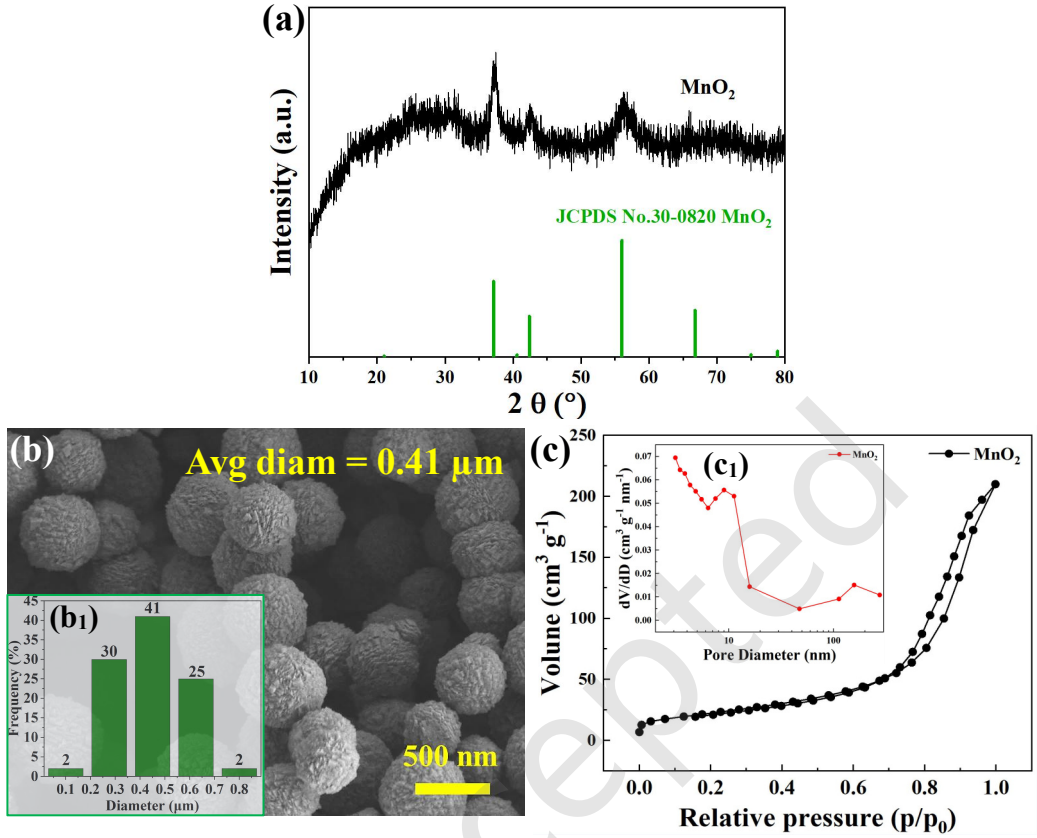

Fig. S4. XRD pattern (a), SEM image (b), nitrogen adsorption/desorption isotherms (c) of the MnO_2 submicron-spheres and their corresponding diameter distribution (b_1) as well as pore diameter distribution (c_1). Mass ratio of SDS to $MnSO_4 \cdot H_2O$ = 50 wt%, volume ratio of EtOH to H_2O = 1:3.

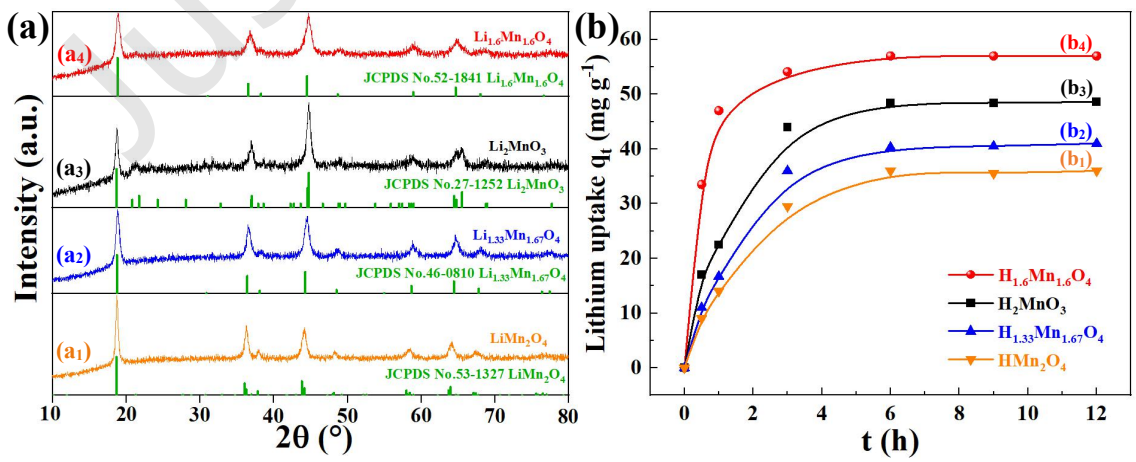

Fig. S5. XRD patterns (a) of the lithium ion-sieve precursors $LiMn_2O_4$ (a_1), $Li_{1.33}Mn_{1.67}O_4$ (a_2), Li_2MnO_3 (a_3) and $Li_{1.6}Mn_{1.6}O_4$ (a_4). Variation in the lithium uptake q_t with time (b) of their corresponding lithium ion-sieves HMn_2O_4 (b_1), $H_{1.33}Mn_{1.67}O_4$ (b_2), H_2MnO_3 (b_3) and $H_{1.6}Mn_{1.6}O_4$ (b_4). Mass of the adsorbent (g): 0.2; volume of the lithium solution (mL): 100; pH of the lithium solution:12.0; initial concentration of the lithium solution (g L^{-1}): 1.8; temperature (ºC): 35.

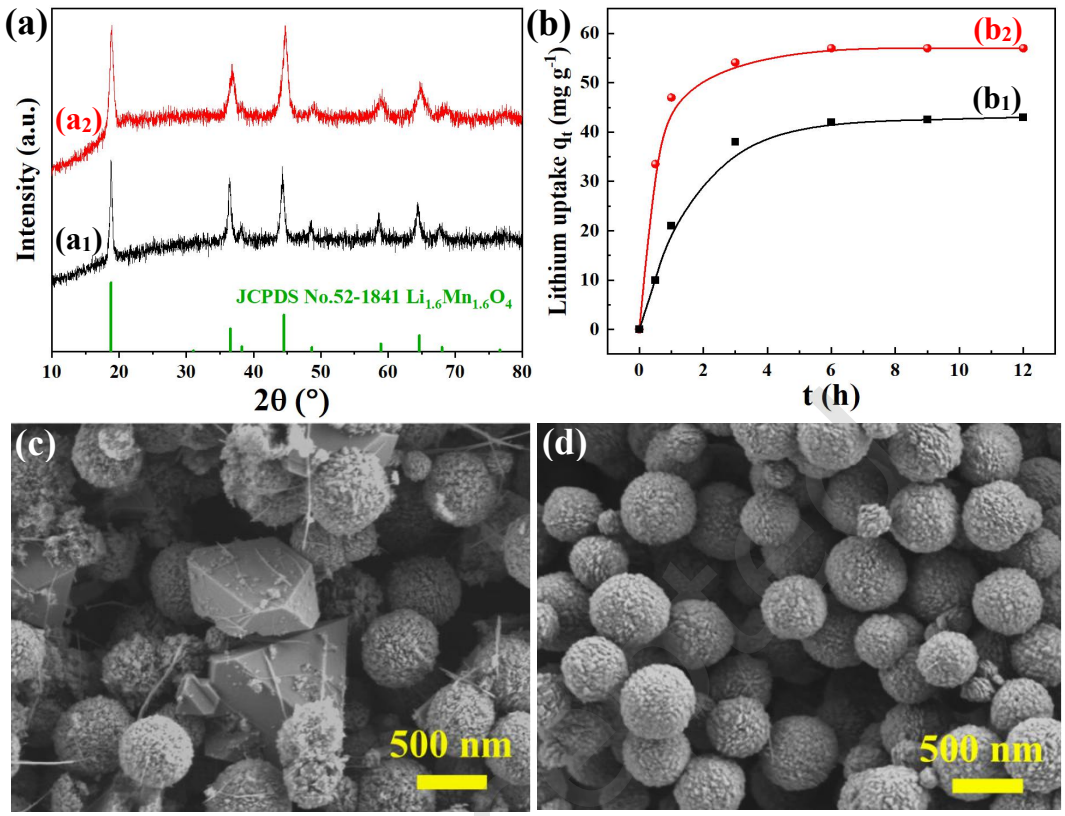

Fig. S6. XRD patters (a) of the lithium ion-sieve precursors LMO-Li_2CO_3 (a_1) and LMO-LiOH (a_2). Variation in the lithium uptake q_t with time (b), SEM images (c, d) of the corresponding lithium ion-sieves HMO-Li_2CO_3 (b_1, c) and HMO-LiOH (b_2, d). Mass of the adsorbent (g): 0.2; volume of the lithium solution (mL): 100; pH of the lithium solution:12.0; initial concentration of the lithium solution (g L^{-1}): 1.8; temperature (ºC): 35.

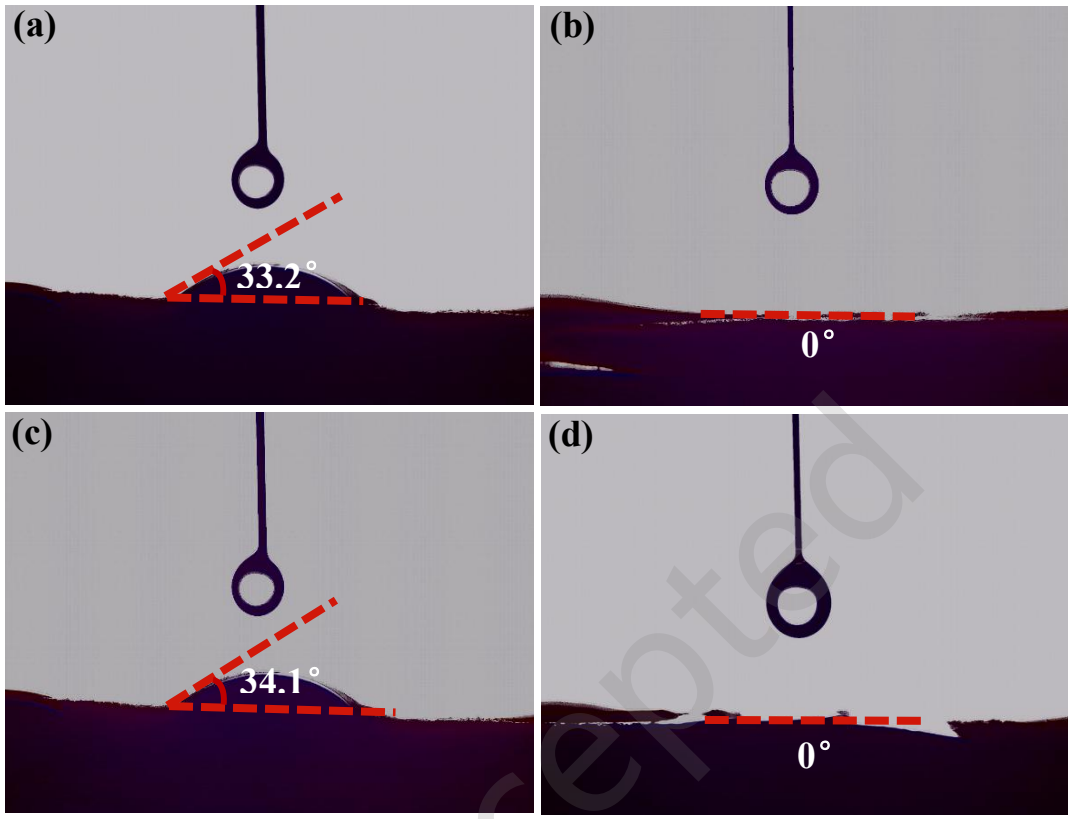

Fig. S7. Surface water contact angles of the lithium ion-sieves HMO-Nothing (a), HMO-SDS (b), HMO-EtOH (c) and HMO-EtOH & SDS (d).

Table S1. Specific surface area, average pore diameter and total pore volume of the MnO_2 microspheres.

Sample	S_{BET} ($m^2 g^{-1}$)	Average pore diameter (nm)	Total pore volume ($cm^3 g^{-1}$)
MnO_2	168.61	38.22	3.15

Table S2. Comparison of the structure and Mn valence for the four lithium ion-sieve precursors $LiMn_2O_4$, $Li_{1.33}Mn_{1.67}O_4$, Li_2MnO_3 and $Li_{1.6}Mn_{1.6}O_4$.

Samples	Structure	Valence of Mn	Ref.
$LiMn_2O_4$	Spinel structure	Mn (Ⅲ) & Mn (Ⅳ)	[39]
$Li_{1.33}Mn_{1.67}O_4$	Spinel structure	Mn (Ⅳ)	[40]
Li_2MnO_3	layered structure	Mn (Ⅳ)	[41]
$Li_{1.6}Mn_{1.6}O_4$	Spinel structure	Mn (Ⅳ)	[35]

Table S3. Specific surface area, average pore diameter and total pore volume of the lithium ion-sieves HMO-Nothing, HMO-SDS, HMO-EtOH, and HMO-EtOH & SDS.

Samples	S_{BET} ($m^2 g^{-1}$)	Average pore diameter (nm)	Total pore volume ($cm^3 g^{-1}$)
HMO-Nothing	27.84	4.35	0.1406
HMO-SDS	40.37	10.98	0.1537
HMO-EtOH	60.66	20.12	0.1715
HMO-EtOH & SDS	120.06	24.68	0.1748

Table S4. The pseudo-first-order and pseudo-second-order kinetics models deployed for the Li^+ adsorption onto the lithium ion-sieve HMO-EtOH & SDS.

Sample	q_e	PFO			PSO		
	($mg\ g^{-1}$)	q_{e1} ($mg\ g^{-1}$)	k_1 (h^{-1})	R^2	q_{e2} ($mg\ g^{-1}$)	k_2 ($g\ mg^{-1}\ h^{-1}$)	R^2
HMO-EtOH & SDS	56.71	40.74	0.8222	0.9766	57.83	0.0907	0.9983

Table S5. Parameters of the intra-particle diffusion model employed for the Li^+ adsorption onto the lithium ion-sieve HMO-EtOH & SDS.

Sample	K_{d1} ($mg\ (g\ h^{1/2})^{-1}$)	K_{d2} ($mg\ (g\ h^{1/2})^{-1}$)	K_{d3} ($mg\ (g\ h^{1/2})^{-1}$)	I_1 ($mg\ g^{-1}$)	I_2 ($mg\ g^{-1}$)	I_3 ($mg\ g^{-1}$)
HMO-EtOH & SDS	49.16	8.08	0.29	3.56	38.21	56.57

Table S6. XPS analysis results of the lithium ion-sieve precursor LMO-EtOH & SDS and corresponding lithium ion-sieve HMO-EtOH & SDS.

Samples	B. E. (eV)	Chemical valence state	Mn (Ⅲ) : Mn (Ⅳ)	Average valence
LMO-EtOH & SDS	643.23	Mn (Ⅳ)	28.07: 71.93	3.72
	642.34	Mn (Ⅲ)		
HMO-EtOH & SDS	643.23	Mn (Ⅳ)	20.74: 79.26	3.79
	642.34	Mn (Ⅲ)		